Journal of Computational Physics **174,** 38–80 (2001)
doi:10.1006/jcph.2001.6873, available online at http://www.idealibrary.com on IDEAL®

Methods for the Accurate Computations of Hypersonic Flows

I. AUSMPW+ Scheme

Kyu Hong Kim, Chongam Kim, and Oh-Hyun Rho

Department of Aerospace Engineering, Seoul National University, Seoul 151-742, South Korea

Received August 23, 1999; revised January 10, 2001

In order to overcome some difficulties observed in the computation of hypersonic flows, a robust, accurate and efficient numerical scheme based on AUSM-type splitting is developed. Typical symptoms appearing in the application of AUSM-type schemes for high-speed flows, such as pressure wiggles near a wall and overshoots across a strong shock, are cured by introducing weighting functions based on pressure (AUSMPW). A newly improved version of the AUSMPW scheme, called AUSMPW+, is developed to increase the accuracy and computational efficiency of AUSMPW in capturing an oblique shock without compromising robustness. With a new definition of the numerical speed of sound at a cell interface, capturing an oblique shock is remarkably enhanced, and it can be proved that an unphysical expansion shock is completely excluded. With simple Mach number interpolation functions, AUSMPW+ is efficient to implement. Extensive numerical tests from supersonic frozen flows to hypersonic nonequilibrium flows validate that the AUSMPW+ scheme provides accurate solutions for the computation of high-speed flows.

Key Words: AUSMPW+; AUSMPW; AUSM+; oblique shock; accuracy; robustness; efficiency; hypersonic flows; equilibrium gas; nonequilibrium gas.

1. INTRODUCTION

With the practical need for efficient hypersonic vehicle design, there has been continuous research to unveil the physics of hypersonic flows experimentally or numerically. It is believed that a full-scale hypersonic vehicle will be developed in the early 21st century. At a pace with this research, much effort has been put into the analysis of hypersonic flows using CFD. Methods developed for the analysis of subsonic or supersonic flows have been extended to hypersonic flow. Up to now, however, these methods do not

0021-9991/01 $35.00

seem to provide satisfactory results compared with those of subsonic or supersonic flows. This is mainly due to the characteristics of high-enthalpy flows involving complex gas reactions.

High-enthalpy flows commonly involve complex physical phenomena including chemical reactions, ionization, vibration of molecules, and radiation. Thus the proper modeling of high-enthalpy flows is essential for an accurate numerical simulation. Although mechanisms of many chemical reactions are well understood, it is still difficult to predict accurate distributions of chemical species in flows involving strong interactions between vibrations and chemical reactions. Turbulence phenomena at high pressure and temperature, involving several molecular species, are not well known either. Turbulence combined with spalled particles produced by abrasion from the surface of a hypersonic vehicle makes flow analysis extremely difficult [1].

Aside from problems of physical modeling, the issue of proper numerical modeling poses challenges, especially for the treatment of errors related to spatial discretization and grid distribution, which is the focus of the present work.

A spatial discretization method should maintain a high level of accuracy, robustness, and efficiency to be applied to hypersonic flows. Hypersonic flow problems generally include severe viscous dissipation in a boundary layer and strong shock waves leading to the large gradient of flow properties. For the accurate calculation of stiff gradient regions, numerical dissipation has to be minimized. Insufficient numerical dissipation, however, induces numerical instability while excessive numerical dissipation easily contaminates physical dissipation. Once unphysical oscillations appear in hypersonic flows, they directly influence the robustness, accuracy, and efficiency of a solver. Numerical instability generally increases in proportion to the local Mach number, and as a result, negative density, pressure, and/or energy are easily produced. Spatial accuracy can deteriorate since it cannot locally be better than the first order to avoid unphysical oscillations due to the monotonicity constraint. Grid systems for hypersonic flow are commonly required to be denser than those for subsonic or supersonic flow to calculate stiff gradient regions accurately, which limits the time step due to the CFL condition and takes requires additional computational time for a solution to converge. Moreover, the source term from chemical reactions poses an additional barrier to efficient computation.

Although several schemes have been developed to cope with these difficulties and have been applied to various hypersonic flow problems, their performances still seem to be unsatisfactory. Today, upwind-biased schemes are the main trend of spatial discretization, which may be categorized as either FVS (flux vector splitting) or FDS (flux difference splitting). FVS, such as Steger–Warming's [2] or Van Leer's [3], has advantages in view of robustness and efficiency. It can be proved that these types of FVS schemes are positively conservative under a CFL-like condition [4], which is very desirable for simulating high-speed flows involving strong shocks and expansions. However, it is also well known that these schemes have accuracy problems in resolving shear layer regions due to excessive numerical dissipation, which occurs more seriously in hypersonic flow. Much effort has spent on developing improved FVS-type schemes for high-speed flows, and they have shown reasonable enhancement in accuracy. In contrast, FDS, which exploits the solution of the local Riemann problem, usually provides accurate solutions. Roe's FDS [5] has a matrix that becomes zero at a sonic transition point and a contact discontinuity. Thus it is able to capture a shock and resolve the shear layer region very accurately. Unfortunately, it has several robustness problems such as the violation of the entropy condition, failure of

local linearization, and appearance of carbuncles [6]. Those defects become more serious in hypersonic flow than in subsonic or supersonic flow. Although an entropy fix may enhance the robustness, a large amount of entropy fix is usually required in hypersonic flow, which requires extra numerical dissipation. This also may cause a decrease of the total enthalpy behind a shock wave and the inaccurate estimation of the surface heating rate. Determining the optimal amount of entropy fix without compromising accuracy is difficult and depends highly on the user's experience. Some variants of Roe's FDS such as Harten–Lax–van Leer's (HLLE) [7] increase the robustness of Roe's FDS at the expense of accuracy. Therefore, contemporary concern is shifted toward combining the accuracy of FDS and the robustness of FVS.

In an effort to design a numerical scheme to meet this concern, the AUSM (advection upstream splitting method) [8] was proposed by Liou and Steffen. In AUSM a cell-interface advection Mach number is appropriately defined to determine upwind extrapolation for convective quantities. As a result, AUSM is accurate enough to resolve a shear layer, and it is simple and robust. Thus AUSM possesses the merits suitable for the analysis of hypersonic flows. However, the characteristic of advection in AUSM may induce the oscillations of flow properties. Successively updated AUSM-type schemes such as AUSMD/V [9] and AUSM+ [10] did not overcome the problem perfectly. AUSMD/V eliminates numerical oscillations or overshoots behind shock waves, though not completely, but may exhibit carbuncle phenomena. AUSM+ eliminates carbuncle phenomena but still shows numerical overshoots behind strong shock waves and oscillations near the region of small convection velocity or pressure gradient, such as near a wall or around a stagnation point. It was observed that oscillations of AUSM-type schemes could be cured by introducing weighting functions based on pressure, leading to the development of AUSMPW (AUSM by pressure-based weight functions) [11, 12]. AUSMPW was found to possess many desirable features such as no carbuncle phenomena, elimination of overshoots, accurate numerical dissipation, and preservation of the total enthalpy. Depending on the particular version, LDFSS (low diffusion flux-splitting schemes) proposed by Edwards did not show oscillations near a strong shock or carbuncle phenomena. But the two problems do not seem to be cured simultaneously [13].

In the present paper, a remedy for the issue related to the accurate discretization for computations of hypersonic flows is proposed by developing a new spatial discretization scheme, named AUSMPW+. AUSMPW+ is designed to increase the accuracy and efficiency of its predecessors by introducing a new numerical speed of sound and by simplifying AUSMPW. AUSMPW+ has higher resolutions in capturing oblique shocks than any other AUSM-type scheme and eliminates the unphysical expansion shocks observed in AUSM+, AUSMPW, or Roe's FDS. Furthermore, the AUSMPW+ scheme is more efficient to implement than AUSMPW while maintaining the same level of the robustness and accuracy.

The present paper is organized as follows. A brief description on the governing equations of a calorically perfect gas and equilibrium and nonequilibrium gases is given in Section 2. In Sections 3 and 4, AUSMPW+ is introduced and the characteristics of the scheme are analyzed in detail. In Section 5, the temporal discretization adopted is briefly explained. Numerous test cases from frozen flows to nonequilibrium flows are presented to verify the properties of AUSMPW+ in Section 6. Finally, conclusions based on the results of the previous sections are drawn in Section 7.

2. GOVERNING EQUATIONS

The two-dimensional Navier–Stokes equations in a conservation form can be expressed as

$$\frac{\partial \boldsymbol{Q}}{\partial t} + \frac{\partial \boldsymbol{E}}{\partial x} + \frac{\partial \boldsymbol{F}}{\partial y} = \left(\frac{\partial \boldsymbol{E_v}}{\partial x} + \frac{\partial \boldsymbol{F_v}}{\partial y} \right) + \boldsymbol{S}, \tag{1}$$

where the flow and flux vectors are

$$\boldsymbol{Q} = \begin{pmatrix} \rho \\ \rho u \\ \rho v \\ \rho e_t \end{pmatrix}, \quad \boldsymbol{E} = \begin{pmatrix} \rho u \\ \rho u^2 + p \\ \rho uv \\ (\rho e_t + p)u \end{pmatrix}, \quad \boldsymbol{F} = \begin{pmatrix} \rho v \\ \rho vu \\ \rho v^2 + p \\ (\rho e_t + p)v \end{pmatrix},$$
$$\boldsymbol{E_v} = \begin{pmatrix} 0 \\ \tau_{xx} \\ \tau_{xy} \\ e_v \end{pmatrix}, \quad \boldsymbol{F_v} = \begin{pmatrix} 0 \\ \tau_{xy} \\ \tau_{yy} \\ f_v \end{pmatrix}, \tag{2}$$

with $e_v = u\tau_{xx} + v\tau_{xy} - q_x$, $f_v = u\tau_{xy} + v\tau_{yy} - q_y$. $\boldsymbol{S}$ represents the source term for thermochemical phenomena. Depending on the treatment of the reaction effect of air molecules, three types of gas can be considered.

For a calorically perfect gas that does not include the effect of vibration or chemical reaction, the equation of state is given by

$$p = (\gamma - 1)\rho e = (\gamma - 1)\rho \left(e_t - \frac{1}{2}(u^2 + v^2) \right), \tag{3}$$

with $\gamma = 1.4$ for air.

For an equilibrium gas where the characteristic time scale of reaction is much shorter than that of fluid, the equation of state has the same form as Eq. (3) with variable specific heat ratio $\tilde{\gamma}$:

$$p = (\tilde{\gamma} - 1)\rho e = (\tilde{\gamma} - 1)\rho \left(e_t - \frac{1}{2}(u^2 + v^2) \right). \tag{4}$$

$\tilde{\gamma}$ in Eq. (4) is the function of two thermodynamic variables. Thermodynamic variables and transport coefficients are calculated using the curve-fitted data in Refs. [14, 15].

For a nonequilibrium gas, all the species and vibrational energy equations must be included to describe the reaction process, and the equation of state is

$$p = \sum_s \rho_s \frac{R}{M_s} T, \tag{5}$$

where R is the universal gas constant (8.314 kJ/kg · mol · K) and M_s is the molecular weight of each species in the nonequilibrium gas. In order to calculate nonequilibrium effects, five species of chemical reaction models are used in the temperature range of $2500 < T < 9000$ K

$$\mathrm{O_2} + M \leftrightarrow \mathrm{O} + \mathrm{O} + M,$$
$$\mathrm{N_2} + M \leftrightarrow \mathrm{N} + \mathrm{N} + M,$$

$$\begin{aligned} \mathrm{NO} + M &\leftrightarrow \mathrm{N} + \mathrm{O} + M, \\ \mathrm{O} + \mathrm{NO} &\leftrightarrow \mathrm{N} + \mathrm{O}_2, \\ \mathrm{O} + \mathrm{N}_2 &\leftrightarrow \mathrm{N} + \mathrm{NO}, \end{aligned} \tag{6}$$

where M can be any one of the five possible collision partners. Considering the species continuity and vibrational energy equations, the flow and flux vectors of Eq. (2) become

$$\boldsymbol{Q} = \begin{pmatrix} \rho \\ \rho u \\ \rho v \\ \rho e_t \\ \rho_1 \\ \rho_2 \\ \rho_3 \\ \rho e_{vib,3} \\ \rho e_{vib,4} \\ \rho e_{vib,5} \end{pmatrix}, \quad \boldsymbol{E} = \begin{pmatrix} \rho u \\ \rho u^2 + p \\ \rho u v \\ (\rho e_t + p)u \\ \rho_1 u \\ \rho_2 u \\ \rho_3 u \\ \rho e_{vib,3} u \\ \rho e_{vib,4} u \\ \rho e_{vib,5} u \end{pmatrix}, \quad \boldsymbol{F} = \begin{pmatrix} \rho v \\ \rho u v \\ \rho v^2 + p \\ (\rho e_t + p)v \\ \rho_1 v \\ \rho_2 v \\ \rho_3 v \\ \rho e_{vib,3} v \\ \rho e_{vib,4} v \\ \rho e_{vib,5} v \end{pmatrix},$$

$$\boldsymbol{S} = \begin{pmatrix} 0 \\ 0 \\ 0 \\ 0 \\ \dot{w}_1 \\ \dot{w}_2 \\ \dot{w}_3 \\ \rho \dot{e}_{vib,3} + \dot{w}_3 e_{vib,3} \\ \rho \dot{e}_{vib,4} + \dot{w}_4 e_{vib,4} \\ \rho \dot{e}_{vib,5} + \dot{w}_5 e_{vib,5} \end{pmatrix}, \quad \boldsymbol{E_v} = \begin{pmatrix} 0 \\ \tau_{xx} \\ \tau_{xy} \\ e_v \\ \rho D_1 \frac{\partial c_1}{\partial x} \\ \rho D_2 \frac{\partial c_2}{\partial x} \\ \rho D_3 \frac{\partial c_3}{\partial x} \\ \rho e_{vib,3} D_3 \frac{\partial c_3}{\partial x} + \kappa_{vib,3} \frac{\partial T_{vib,3}}{\partial x} \\ \rho e_{vib,4} D_4 \frac{\partial c_4}{\partial x} + \kappa_{vib,4} \frac{\partial T_{vib,4}}{\partial x} \\ \rho e_{vib,5} D_5 \frac{\partial c_5}{\partial x} + \kappa_{vib,5} \frac{\partial T_{vib,5}}{\partial x} \end{pmatrix},$$

$$\boldsymbol{F_v} = \begin{pmatrix} 0 \\ \tau_{xy} \\ \tau_{yy} \\ f_v \\ \rho D_1 \frac{\partial c_1}{\partial y} \\ \rho D_2 \frac{\partial c_2}{\partial y} \\ \rho D_3 \frac{\partial c_3}{\partial y} \\ \rho e_{vib,3} D_3 \frac{\partial c_3}{\partial y} + \kappa_{vib,3} \frac{\partial T_{vib,3}}{\partial y} \\ \rho e_{vib,4} D_4 \frac{\partial c_4}{\partial y} + \kappa_{vib,4} \frac{\partial T_{vib,4}}{\partial y} \\ \rho e_{vib,5} D_5 \frac{\partial c_5}{\partial y} + \kappa_{vib,5} \frac{\partial T_{vib,5}}{\partial y} \end{pmatrix}. \tag{7}$$

$\boldsymbol{S}$ is the source term that includes $\dot{w}_i$ in the species continuity equations and $(\rho\dot{e}_{vib,i} + \dot{w}_i e_{vib,i})$ in the vibrational energy equations of each species. As shown in Eq. (7), the four-temperature model is adopted to test the robustness of AUSMPW+ in nonequilibrium problems involving highly dissociated flow and low density of diatomic molecules. Reaction rate constants and transport coefficients are calculated according to Refs. [16, 17].

3. SPATIAL DISCRETIZATION

3.1. Proposed Scheme: AUSMPW+

In AUSM-type schemes, an advection Mach number at a cell interface is defined to determine an upwind extrapolation for convective quantities. Although the usage of the advection Mach number yields a notable improvement in accuracy, it may also induce spurious oscillatory phenomena. AUSM+, for example, shows oscillations near a wall and across a shock. The numerical flux of AUSM+ at a cell interface is given by

$$\boldsymbol{F}_{\frac{1}{2},AUSM+} = \left(M_L^+\big|_{\beta=\frac{1}{8}} + M_R^-\big|_{\beta=\frac{1}{8}}\right) c_{\frac{1}{2}} \boldsymbol{\Phi}_L + \left(P_L^+\big|_{\alpha=\frac{3}{16}} \boldsymbol{P}_L + P_R^-\big|_{\alpha=\frac{3}{16}} \boldsymbol{P}_R\right), \tag{8}$$

if $m_{1/2} = M_L^+ + M_R^- > 0$. $\boldsymbol{\Phi} = (\rho, \rho u, \rho H)^T$, and $\boldsymbol{P} = (0, p, 0)^T$. The subscripts $1/2$ and (L, R) stand for a quantity at a cell interface and at the left and right states across a cell interface, respectively. The split Mach number and pressure of AUSM+ across a cell interface are given by

$$M^{\pm}|_{\beta} = \begin{cases} \pm\frac{1}{4}(M \pm 1)^2 \pm \beta(M^2-1)^2, & |M| \le 1, \\ \frac{1}{2}(M \pm |M|), & |M| > 1, \end{cases} \tag{9}$$

$$P^{\pm}|_{\alpha} = \begin{cases} \frac{1}{4}(M \pm 1)^2(2 \mp M) \pm \alpha M(M^2-1)^2, & |M| \le 1, \\ \frac{1}{2}(1 \pm \mathrm{sign}(M)), & |M| > 1. \end{cases} \tag{10}$$

The Mach number of each side is defined as

$$M_{L,R} = \frac{U_{L,R}}{c_{\frac{1}{2}}}, \quad c_{\frac{1}{2}} = \min(\tilde{c}_L, \tilde{c}_R), \tag{11}$$

where $\tilde{c} = c^{*^2}/[\max(|U|, c^*)]$ and the critical speed of sound c^* is given by

$$\sqrt{\frac{2(\gamma-1)}{(\gamma+1)} H}$$

from the isoenergetic condition. H is the total enthalpy and U is the velocity component normal to a cell interface.

As can be seen from Eq. (8), AUSM+ considers the one-side convection quantity $\boldsymbol{\Phi}_L$ only according to the sign of a cell-interface Mach number $(m_{1/2})$. This is thought to yield oscillations because considering the one-side quantity only is unsuitable for the flow physics in subsonic regions. Other phenomena that are frequently seen in AUSM-type schemes are oscillations across a shock. Although the reflection of only a one-side quantity produces some disadvantages as mentioned above, it is also useful in the sense that AUSM-type schemes with an advection Mach number can capture a stationary shock or contact

discontinuity through one cell interface. Thus it is intended to carefully control the advection property of AUSM+ by employing both-side quantities to remove oscillatory phenomena while maintaining the original advantages of AUSM+ in accuracy, efficiency, and robustness. In these respects, the AUSMPW+ scheme is designed to control the advection property by introducing pressure-based weighting functions f and w only in the problematic regions such as a shock or a boundary layer. The improvement of AUSMPW+ consists of three parts. The first is the introduction of a new definition of the numerical speed of sound for high resolution in capturing an oblique shock. The second is the elimination of the physically unacceptable expansion shock which is observed in AUSM+, AUSMPW+, or Roe's FDS. The last is to simplify AUSMPW to enhance computational efficiency. For the purpose of clear presentation, AUSMPW is briefly introduced.

3.1.1. *AUSMPW (AUSM by Pressure-Based Weight Function)*

The main feature of AUSMPW is the removal of the oscillations of AUSM+ [10] near a wall or across a strong shock by introducing pressure-based weight functions. AUSMPW uses the pressure-based weight function f to treat the oscillations near a wall and w to remove the oscillation across a strong shock. The starting point of AUSMPW is to observe the fact that AUSM+ and AUSMD [9] are complementary to each other. AUSM+ has no carbuncle phenomena but shows numerical oscillations near a wall while AUSMD has no numerical oscillations near a wall but shows carbuncle phenomena. This difference can be seen by examining the mass fluxes of AUSM+ and AUSMD,

$$\rho u_{\frac{1}{2},AUSM+} = M_L^+ c_{\frac{1}{2}} \rho_L + M_R^- c_{\frac{1}{2}} \rho_L, \quad m_{\frac{1}{2}} \geq 0, \tag{12}$$

$$\rho u_{\frac{1}{2},AUSMD} = M_L^+ c_{\frac{1}{2}} \rho_L + M_R^- c_{\frac{1}{2}} \rho_R, \quad \rho m_{\frac{1}{2}} \geq 0, \tag{13}$$

where $m_{1/2} = M_L^+ + M_R^-$ and $\rho m_{1/2} = \rho_L M_L^+ + \rho_R M_R^-$.

From Eqs. (12) and (13), it can be noticed that AUSM+ considers the left cell density only while AUSMD takes both cell densities. This is thought to be the reason for the numerical oscillations of AUSM+ and carbuncle phenomena of AUSMD. In order to summon AUSM+ and AUSMD, the density ratio is multiplied by the second term of Eq. (12) as follows:

$$\rho u_{\frac{1}{2},AUSMPW} = M_L^+ c_{\frac{1}{2}} \rho_L + M_R^- c_{\frac{1}{2}} \rho_L \left(\frac{\rho_R}{\rho_L} \right). \tag{14}$$

With the equation of state applied to the speed of sound, the density is given by

$$\rho = \gamma \frac{p}{c^2}. \tag{15}$$

If the values of the specific heat ratio and the speed of sound are chosen at a cell interface, Eq. (14) becomes

$$\rho u_{\frac{1}{2},AUSMPW} = M_L^+ c_{\frac{1}{2}} \rho_L + M_R^- c_{\frac{1}{2}} \rho_L \frac{\gamma_s \frac{p_R}{c_s^2}}{\gamma_s \frac{p_L}{c_s^2}}, \tag{16}$$

$$\rho u_{\frac{1}{2},AUSMPW} = M_L^+ c_{\frac{1}{2}} \rho_L + \frac{p_R}{p_L} M_R^- c_{\frac{1}{2}} \rho_L. \tag{17}$$

By introducing p_R/p_L, AUSMPW considers the right cell property p_R, which prevents the numerical oscillations near a wall. For symmetric representation, Eq. (17) is modified as [11]

$$\rho u_{\frac{1}{2},AUSMPW} = \frac{p_L}{p_s} M_L^+ c_{\frac{1}{2}} \rho_L + \frac{p_R}{p_s} M_R^- c_{\frac{1}{2}} \rho_L, \tag{18}$$

or

$$\begin{aligned} \rho u_{\frac{1}{2},AUSMPW} &= \left(M_L^+ c_{\frac{1}{2}} \rho_L + M_R^- c_{\frac{1}{2}} \rho_L\right)_{AUSM^+} + \left(\frac{p_L}{p_s} - 1\right) M_L^+ c_{\frac{1}{2}} \rho_L + \left(\frac{p_R}{p_s} - 1\right) M_R^- c_{\frac{1}{2}} \rho_L \\ &= \left(M_L^+ c_{\frac{1}{2}} \rho_L + M_R^- c_{\frac{1}{2}} \rho_L\right)_{AUSM^+} + f_L M_L^+ c_{\frac{1}{2}} \rho_L + f_R M_R^- c_{\frac{1}{2}} \rho_L, \end{aligned} \tag{19}$$

where

$$f_{L,R} = \begin{cases} \frac{p_{L,R}}{p_s} - 1, |M_{L,R}| < 1, & p_s \neq 0 \\ 0, & \text{elsewhere} \end{cases}$$

and

$$p_s = P_L^+\big|_{\alpha=\frac{3}{16}} p_L + P_R^-\big|_{\alpha=\frac{3}{16}} p_R.$$

Equation (19) takes the same form as AUSM+ in the supersonic region ($f_{L,R} = 0$). The choice for p_s prevents the unwanted interference of $f_{L,R}$ across a shock wave and maintains the symmetric and continuous transition of p_s as the Mach number goes to zero asymptotically. Although the modified flux of Eq. (19) does not show an oscillatory behavior near a wall, it may have a problem in accuracy, particularly in boundary layers and shock regions due to the increase of $f_L M_L^+ + f_R M_R^-$. For example, when the Mach number increases form zero to one, M_L^+ does not become zero as can be seen from Eq. (9). Thus $f_L M_L^+$ remains active inside a boundary layer or in shock regions and provides extra numerical dissipation. As another side effect, it has the potential to induce shock instability causing carbuncle phenomena since Eq. (19) possesses the numerical dissipation term in proportion to the pressure difference [18]. These problems were cured by carefully limiting $f_{L,R}$ to

$$f_{L,R} = \begin{cases} \left(\frac{p_{L,R}}{p_s} - 1\right) pl(p_{L,R}, p_{R,L}) |M_{L,R}^{\pm}|_{\beta=0}| \times \min\left(1, \left(\frac{|\bar{V}_{L,R}|}{c_{\frac{1}{2}}}\right)^{0.25}\right), & |M_{L,R}| \leq 1, \\ 0, & |M_{L,R}| > 1, \end{cases} \tag{20}$$

where

$$pl(x, y) = \begin{cases} 4 \cdot \min\left(\frac{x}{y}, \frac{y}{x}\right) - 3, & \frac{3}{4} \leq \min\left(\frac{x}{y}, \frac{y}{x}\right) < 1, \\ 0, & 0 \leq \min\left(\frac{x}{y}, \frac{y}{x}\right) < \frac{3}{4}. \end{cases}$$

Second, the numerical oscillations near a shock wave or the region of a stiff gradient have to be examined. AUSM+, which considers the one-side property according to the

sign of a cell-interface Mach number, may yield excessive or insufficient numerical fluxes, especially in a non-shock-aligned grid system. This produces oscillations of flow properties. In AUSMPW, both properties across a cell interface are considered through another pressure-based weight function w,

$$\rho u_{\frac{1}{2},AUSMPW} = (1+f_L)M_L^+\big|_{\beta=\frac{1}{8}} c_{\frac{1}{2}}\rho_L + (1+f_R)M_R^-\big|_{\beta=\frac{1}{8}} c_{\frac{1}{2}}((1-w)\cdot\rho_L + w\cdot\rho_R), \quad (21)$$

where

$$w(p_L, p_R) = 1 - \min\left(\frac{p_L}{p_R}, \frac{p_R}{p_L}\right)^3.$$

From the form of w, it can be noticed that the value of w becomes very small except in the region of a shock discontinuity.

In summary, the numerical flux of AUSMPW is written as

$$\boldsymbol{F}_{\frac{1}{2}} = \bar{M}_L^+ c_{\frac{1}{2}}\boldsymbol{\Phi}_L + \bar{M}_R^- c_{\frac{1}{2}}\boldsymbol{\Phi}_R + \left(P_L^+\big|_{\alpha=\frac{3}{16}}\boldsymbol{P}_L + P_R^-\big|_{\alpha=\frac{3}{16}}\boldsymbol{P}_R\right), \quad (22)$$

where

(i) for $m_{1/2} \geq 0$

$$\bar{M}_L^+ = M_L^+\big|_{\beta=\frac{1}{8}} + M_R^-\big|_{\beta=\frac{1}{8}} - M_R^-\big|_{\beta=\frac{1}{8}} \times w\cdot(1+f_R) + \left(f_L M_L^+\big|_{\beta=\frac{1}{8}} + f_R M_R^-\big|_{\beta=\frac{1}{8}}\right),$$
$$\bar{M}_R^- = M_R^-\big|_{\beta=\frac{1}{8}} \times w\cdot(1+f_R),$$

(ii) for $m_{1/2} < 0$

$$\bar{M}_L^+ = M_L^+\big|_{\beta=\frac{1}{8}} \times w\cdot(1+f_L),$$
$$\bar{M}_R^- = M_L^+\big|_{\beta=\frac{1}{8}} + M_R^-\big|_{\beta=\frac{1}{8}} - M_L^+\big|_{\beta=\frac{1}{8}} \times w\cdot(1+f_L) + \left(f_L M_L^+\big|_{\beta=\frac{1}{8}} + f_R M_R^-\big|_{\beta=\frac{1}{8}}\right),$$

with $\boldsymbol{\Phi} = (\rho, \rho u, \rho H)^T$, and $\boldsymbol{P} = (0, p, 0)^T$. The split Mach number and pressure of AUSMPW at a cell interface are the same as those of AUSM+ in Eqs. (9) and (10). The Mach number on each side of a cell interface is also defined as in Eq. (11).

3.1.2. *AUSMPW+: An Improved Version of AUSMPW*

In the previous section, it was mentioned that $f_L M_L^+|_{\beta=1/8} + f_R M_R^-|_{\beta=1/8}$ of Eq. (22) was designed to remove oscillations near a wall and $M_R^-|_{\beta=1/8} \times w\cdot(1+f_R)$ or $M_L^+|_{\beta=1/8} \times w\cdot(1+f_L)$ was designed to exclude overshoots or oscillations behind strong shocks. In order to maintain the same accuracy level as AUSM+ or Roe's FDS and to reduce shock instability that induces carbuncle phenomena, $pl(p_L, p_R) \times |M_{L,R}^{\pm}|_{\beta=0}| \times \min(1, (\vec{\boldsymbol{V}}_{L,R}/c_{1/2})^{0.25})$, which acts like a limiter of the function $f_{L,R}$, is multiplied to control the magnitude of $f_L M_L^+ + f_R M_R^-$. Without this additional limiting term, the numerical dissipation term, $f_L M_L^+ + f_R M_R^-$, may become much larger, particularly in hypersonic boundary layer, due to the noticeable difference between M_L^+ and M_R^-, which directly influences sensitive aerodynamic coefficients such as the surface heat transfer coefficient. It also gives an adverse effect on accuracy in capturing shock waves because $f_L M_L^+ + f_R M_R^-$ has almost the

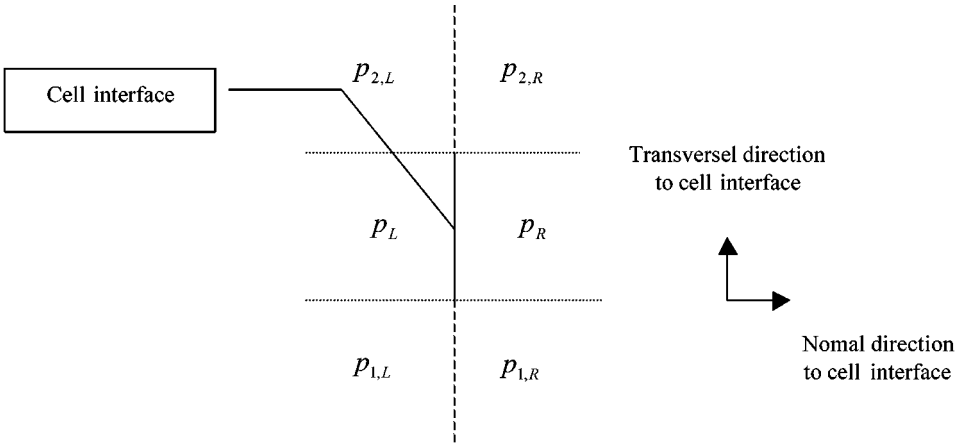

FIG. 1. Pressure distribution around a cell interface.

same order of magnitude as other dissipation terms. The term $M^{\pm}_{L,R}|_{\beta=0}$ is designed to scale down the order of magnitude of $f_{L,R}$, and $\min(1, (|\vec{\boldsymbol{V}}_{L,R}|/c_{1/2})^{0.25})$ makes $f_{L,R}$ vanish in the stagnation region. The function $pl(p_L, p_R)$ is designed such that $f_{L,R}$ becomes zero in large pressure gradient regions.

Although AUSMPW has the merits, it contains a complicating function $f_{L,R}$, which entails extra computational costs. In AUSMPW+, $f_{L,R}$ is modified by considering accuracy, shock instability, and efficiency.

To maintain accuracy in resolving the shear layer and capturing the shock wave, the following approximation is introduced:

$$M^+_L \cong -M^-_R, \quad M \to 0. \tag{23}$$

Then, $f_L M^+_L + f_R M^-_R$ becomes $(f_R - f_L)M^-_R$ when $m_{1/2} \geq 0$, and it decreases in proportion to the Mach number. This obviates the usage of $pl(p_L, p_R) \times |M^{\pm}_{L,R}|_{\beta=0}| \times \min(1, (\vec{\boldsymbol{V}}_{L,R}/c_{1/2})^{0.25})$ in $f_{L,R}$ without introducing excessive numerical dissipation. To remove carbuncle phenomena, however, it is necessary that the function f becomes zero in the region of a strong moving shock. In AUSMPW+, this is achieved by multiplying the term that considers pressures in the transverse direction as shown in Fig. 1. As a result, AUSMPW+ can be summarized as

$$\boldsymbol{F}_{\frac{1}{2}} = \bar{M}^+_L c_{\frac{1}{2}} \boldsymbol{\Phi}_L + \bar{M}^-_R c_{\frac{1}{2}} \boldsymbol{\Phi}_R + \left(P^+_L\big|_{\alpha=\frac{3}{16}} \boldsymbol{P}_L + P^-_R\big|_{\alpha=\frac{3}{16}} \boldsymbol{P}_R \right), \tag{24}$$

where

(i) for $m_{1/2} \geq 0$

$$\bar{M}^+_L = M^+_L + M^-_R \cdot [(1-w)\cdot(1+f_R) - f_L],$$
$$\bar{M}^-_R = M^-_R \cdot w \cdot (1+f_R),$$

(ii) for $m_{1/2} < 0$

$$\bar{M}^+_L = M^+_L \cdot w \cdot (1+f_L),$$
$$\bar{M}^-_R = M^-_R + M^+_L \cdot [(1-w)\cdot(1+f_L) + f_L - f_R)],$$

with

$$w(p_L, p_R) = 1 - \min\left(\frac{p_L}{p_R}, \frac{p_R}{p_L}\right)^3. \tag{25}$$

And $f_{L,R}$ is simplified to

$$f_{L,R} = \begin{cases} \left(\frac{p_{L,R}}{p_s} - 1\right) \min\left(1, \frac{\min(p_{1,L}, p_{1,R}, p_{2,L}, p_{2,R})}{\min(p_L, p_R)}\right)^2, & p_s \neq 0, \\ 0, & \text{elsewhere}, \end{cases} \tag{26}$$

where $p_s = P_L^+ p_L + P_R^- p_R$.

As shown in Eq. (25) the function w goes as the cube of the pressure ratio and has a very small value except at a large pressure gradient region such as a shock. The value of $f_{L,R}$ also becomes very small except at the region where oscillation exists. As a result, AUSMPW+ has the same form as AUSM+ except at a shock or oscillatory region. The accuracy, robustness, efficiency, and convergence characteristics of AUSMPW+ will be examined in detail in Section 4 and 6.

The Mach number and pressure splitting functions of AUSMPW+ at a cell interface are also simplified to

$$M^{\pm} = \begin{cases} \pm\frac{1}{4}(M \pm 1)^2, & |M| \leq 1, \\ \frac{1}{2}(M \pm |M|), & |M| > 1, \end{cases} \tag{27}$$

$$P^{\pm}|_{\alpha} = \begin{cases} \frac{1}{4}(M \pm 1)^2(2 \mp M) \pm \alpha M(M^2 - 1)^2, & |M| \leq 1, \\ \frac{1}{2}(1 \pm \text{sign}(M)), & |M| > 1, \end{cases} \tag{28}$$

where α ranges from 0 to 3/16. When $\alpha = 0$ AUSMPW+ is more robust in view of stability since the pressure splitting function is a little more diffusive.

The Mach number on each side is similarly defined as follows:

$$M_{L,R} = \frac{U_{L,R}}{c_{\frac{1}{2}}}. \tag{29}$$

However, the choice of the speed of sound ($c_{1/2}$) of AUSMPW+ is quite different.

3.1.3. *Numerical Speed of Sound for AUSMPW+*

In AUSM-type schemes, the choice of the numerical speed of sound is crucial since it is closely related to the resolution of physical discontinuities. Using a cell-interface sound speed, Liou suggested the Mach number on each cell side in AUSM+ as in Eq. (11) [10]. Although AUSMPW with the sound speed of Eq. (11) is able to capture a stationary normal shock through one cell interface [11, 12], an oblique shock is smeared over about four cell interfaces in a nonaligned grid system. Even with nearly shock-aligned grids, an oblique shock cannot be captured in one cell interface. Moreover, AUSMPW with the speed of sound based on Eq. (11) cannot distinguish an unphysical expansion shock from a compression shock, thus admitting an entropy-violating solution like AUSM+ or Roe's FDS.

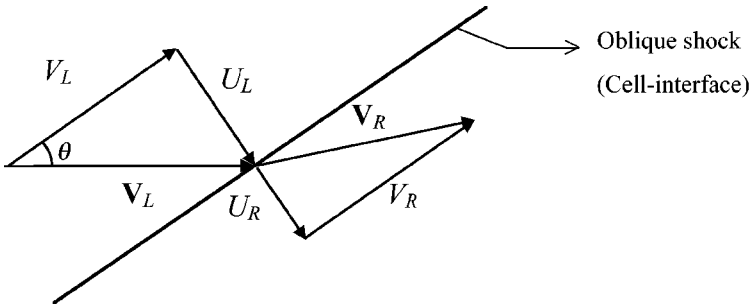

FIG. 2. Schematic of an oblique shock.

In order to improve the capability of capturing an oblique shock and to remove an unphysical expansion shock, the following numerical speed of sound is designed for AUSMPW+. First, the speed of sound is defined according to flow directions to pick out an entropy-decreasing expansion shock. Second, to capture a stationary oblique shock exactly through one cell interface in a shock-aligned grid system, the total enthalpy excluding the tangential velocity component along an oblique shock is used in defining the speed of sound.

Although an oblique shock cannot be captured through one cell interface in case of non-shock-aligned grids, numerical dissipation decreases in proportion to the amount of the tangential velocity component excluded. Thus an oblique shock can be captured more accurately with the present formulation of the speed of sound:

$$\begin{aligned} &\text{(i)} \quad \frac{1}{2}(U_L + U_R) > 0\text{:} \quad c_{\frac{1}{2}} = c_s^2 / \max(|U_L|, c_s), \\ &\text{(ii)} \quad \frac{1}{2}(U_L + U_R) < 0\text{:} \quad c_{\frac{1}{2}} = c_s^2 / \max(|U_R|, c_s). \end{aligned} \tag{30}$$

From the conservation laws normal to an oblique shock and the equation of state for a calorically perfect gas, the speed of sound normal to a cell interface, c_s, is given by

$$c_s = \sqrt{2\,(\gamma - 1)\,/\,(\gamma + 1)\,H_{normal}}, \tag{31}$$

where $H_{normal} = 0.5 \times (H_{total,L} - 0.5 \times V_L^2 + H_{total,R} - 0.5 \times V_R^2)$ (see Fig. 2). Then, we can see that c_s satisfies the Prandtl relation across an oblique shock just like the critical speed of sound (c^*) across a normal shock,

$$\frac{U_L}{c_s} \times \frac{U_R}{c_s} = 1. \tag{32}$$

The speed of sound for reacting gases will be discussed in Section 4.7.

3.2. Higher Order Interpolation

Upwind schemes have in general first-order spatial accuracy. For better accuracy, a MUSCL (monotone upstream-centered schemes for conservation laws) approach using primitive variables is adopted to interpolate higher order left and right states across a cell interface. To monitor the local gradient of a solution and control spatial order, we use

minmod limiter

$$W_L = W_i + \frac{1}{4}[(1-\kappa)\bar{\nabla} + (1+\kappa)\bar{\Delta}]_i, \qquad W_R = W_{i+1} - \frac{1}{4}[(1-\kappa)\bar{\nabla} + (1+\kappa)\bar{\Delta}]_{i+1},$$
$$\bar{\Delta}_i = \min\text{mod}[(W_{i+1} - W_i), \beta(W_i - W_{i-1})],$$
$$\bar{\nabla}_i = \min\text{mod}[(W_i - W_{i-1}), \beta(W_{i+1} - W_i)], \tag{33}$$
$$\min\text{mod}(x, y) = \text{sign}(x)\max[0, \min(x\text{sign}(y), y\text{sign}(x))], \quad 1 \le \beta \le \frac{(3-\kappa)}{(1-\kappa)},$$

where $W = (\rho, u, v, p)^T$. This formulation can produce third-order spatial accuracy if κ is equal to $1/3$.

4. CHARACTERISTICS OF AUSMPW+

In this section, the numerical properties of the AUSMPW+ scheme are analyzed from the viewpoint of the accuracy, robustness, and efficiency.

4.1. Accuracy

Since AUSMPW+ is based on AUSMPW, it exhibits the same accuracy as AUSMPW. Additionally AUSMPW+ increases accuracy in capturing an oblique shock due to the newly proposed speed of sound and less diffusive Mach number and pressure splitting functions. In order to investigate properties of AUSMPW+, we adopt the flux form which shows the numerical dissipation term explicitly,

$$\boldsymbol{F}_{\frac{1}{2}} = \frac{1}{2}[(U_L\boldsymbol{\Phi}_L + U_R\boldsymbol{\Phi}_R) + (\boldsymbol{P_L} + \boldsymbol{P_R})] + \boldsymbol{D}, \tag{34}$$

where $\boldsymbol{D}$ stands for numerical dissipation.

4.1.1. *Stationary Oblique Shock Discontinuity*

The speed of sound used in AUSMPW+ is designed such that the corresponding characteristic Mach number satisfies the Prandtl relation, Eq. (32), across a stationary oblique shock in a shock-aligned grid system. Assuming a cell interface is aligned with a shock as in Fig. 2, the Mach number of AUSMPW+ across a stationary oblique shock is given by

$$M_L = \frac{U_L}{c_{\frac{1}{2}}} = \frac{U_L}{\left(c_s^2/U_L\right)} = \left(\frac{U_L}{c_s}\right)^2,$$
$$M_R = \frac{U_R}{c_{\frac{1}{2}}} = \frac{U_R}{\left(c_s^2/U_L\right)} = \left(\frac{U_L}{c_s}\right)\left(\frac{U_R}{c_s}\right) = 1, \tag{35}$$

when $U_L > U_R$. Then, the flux of AUSMPW+ becomes

$$\boldsymbol{F}_{\frac{1}{2}} = \bar{M}_L^+ c_{\frac{1}{2}}\boldsymbol{\Phi}_L + \bar{M}_R^- c_{\frac{1}{2}}\boldsymbol{\Phi}_R + (P_L^+\boldsymbol{P}_L + P_R^-\boldsymbol{P}_R) = U_L\boldsymbol{\Phi}_L + p_L\vec{\boldsymbol{n}}, \tag{36}$$

if $m_{1/2} \ge 0$. In this case, $\boldsymbol{\Phi} = (\rho, \rho u, \rho v, \rho H)^T$.

Here,

$$\bar{M}_L^+ = M_L^+ + M_R^- \times ((1-w)\cdot(1+f_R) - f_L) = \frac{U_L}{c_{\frac{1}{2}}},$$
$$\bar{M}_R^- = M_R^- \times w \cdot (1+f_R) = 0.$$

Now, if we apply the oblique shock relations,

$$\begin{aligned} &① \ \rho_L U_L = \rho_R U_R, && ② \ \rho_L U_L^2 + p_L = \rho_R U_R^2 + p_R, \\ &③ \ V_L = V_R, && ④ \ H_L = H_R, \\ &⑤ \ u = \sin\theta \cdot U + \cos\theta \cdot V, && ⑥ \ v = -\cos\theta \cdot U + \sin\theta \cdot V, \end{aligned} \tag{37}$$

the numerical dissipation of AUSMPW+ becomes

$$\begin{aligned} \boldsymbol{D}|_1 &= -\frac{1}{2}(\rho_R U_R - \rho_L U_L) = 0, \\ \boldsymbol{D}|_2 &= -\frac{1}{2}(\rho_R u_R U_R - \rho_L u_L U_L + (p_R - p_L)\cdot\sin\theta) \\ &= -\frac{1}{2}((\rho_R U_R U_R - \rho_L U_L U_L + p_R - p_L)\cdot\sin\theta + (\rho_R V_R U_R - \rho_L V_L U_L)\cdot\cos\theta) \\ &= 0, \\ \boldsymbol{D}|_3 &= -\frac{1}{2}(\rho_R v_R U_R - \rho_L v_L U_L + (p_R - p_L)\cdot(-\cos\theta)) \\ &= -\frac{1}{2}((\rho_R U_R U_R - \rho_L U_L U_L + p_R - p_L)\cdot(-\cos\theta) + (\rho_R V_R U_R - \rho_L V_L U_L)\cdot\sin\theta) \\ &= 0, \\ \boldsymbol{D}|_4 &= -\frac{1}{2}\rho_L U_L (H_R - H_L) = 0. \end{aligned} \tag{38}$$

Thus all AUSMPW+ dissipation terms become zero. This means that AUSMPW+ can capture a stationary oblique shock without numerical diffusion in a shock-aligned grid system. It is important to note that the dissipation terms of AUSMPW+ do not contain the pressure-based weight functions f and w. This implies that f and w are active in removing oscillations only in a non-shock-aligned grid system and that the resolution of a shock discontinuity is independent of f and w in a shock-aligned grid system. Also note that AUSMPW+ with various forms of f and w, such as the vector form of f and w, can yield a more appropriate form of numerical dissipation.

4.1.2. *Stationary Contact Discontinuity*

In the region where $M \to 0$, the dissipation terms of AUSMPW+ become

$$\boldsymbol{D}|_{1,2,3} = 0, \tag{39}$$

when $p_L = p_R$.

Thus AUSMPW+, similar to AUSMPW and AUSM+, can calculate a stationary contact discontinuity exactly and does not have any extra dissipation. Moreover, AUSMPW+ may give more accurate solutions in a boundary layer, expansion, and shock regions because the

interpolation function in Eqs. (27) and (28) adopted in AUSMPW+ is less diffusive than those in AUSM+ and AUSMPW.

4.1.3. *Expansion Shock*

The numerical dissipation of Roe's FDS, AUSM+, and AUSMPW across a normal shock can be expressed as follows:

Roe's FDS :

$$\begin{aligned}
\boldsymbol{D}|_1 &= -\frac{1}{2}(\rho_R U_R - \rho_L U_L),\\
\boldsymbol{D}|_2 &= -\frac{1}{2}\left(\rho_R U_R^2 - \rho_L U_L^2 + p_R - p_L\right),\\
\boldsymbol{D}|_3 &= -\frac{1}{2}\frac{U_L U_R}{(\gamma-1)}\left(\rho_R U_R^2 - \rho_L U_L^2 + p_R - p_L\right).
\end{aligned} \tag{40}$$

AUSM+, AUSMPW:

$$\begin{aligned}
\boldsymbol{D}|_1 &= -\frac{1}{2}(\rho_R U_R - \rho_L U_L),\\
\boldsymbol{D}|_2 &= -\frac{1}{2}\left(\rho_R U_R^2 - \rho_L U_L^2 + p_R - p_L\right),\\
\boldsymbol{D}|_3 &= -\frac{1}{2}\rho_L U_L (H_R - H_L).
\end{aligned} \tag{41}$$

AUSMPW+:

for $M_L > 1 > M_R > 0$ (compression shock)

$$\begin{aligned}
\boldsymbol{D}|_1 &= -\frac{1}{2}(\rho_R U_R - \rho_L U_L),\\
\boldsymbol{D}|_2 &= -\frac{1}{2}\left(\rho_R U_R^2 - \rho_L U_L^2 + p_R - p_L\right),\\
\boldsymbol{D}|_3 &= -\frac{1}{2}\rho_L U_L (H_R - H_L);
\end{aligned} \tag{42}$$

for $0 < M_L < 1 < M_R$ (expansion shock)

$$\begin{aligned}
\boldsymbol{D}|_1 &= -\frac{1}{2}(\rho_R U_R - \rho_L U_L) + (M_L^+ - M_L) c_{\frac{1}{2}} \rho_L,\\
\boldsymbol{D}|_2 &= -\frac{1}{2}\left(\rho_R U_R^2 - \rho_L U_L^2 + p_R - p_L\right) + (M_L^+ - M_L) c_{\frac{1}{2}} \rho_L U_L + (P_L^+ - 1) p_L,\\
\boldsymbol{D}|_3 &= -\frac{1}{2}(\rho_R U_R H_R - \rho_L U_L H_L) + (M_L^+ - M_L) c_{\frac{1}{2}} \rho_L H_L.
\end{aligned} \tag{43}$$

Equations (40) and (41) express a stationary normal shock relation. Thus the numerical dissipation becomes zero across a shock discontinuity, which means that Roe's FDS, AUSM+, and AUSMPW schemes can capture a stationary normal shock without numerical dissipation. However, the numerical dissipation terms shown in Eqs. (40) and (41) do not

have a built-in mechanism to distinguish a compression shock from an unphysical expansion shock. For AUSMPW+, the speed of sound which considers flow directions as shown in Eq. (30) distinguishes a compression shock from an expansion shock. Equations (42) and (43) show the numerical dissipation in each case. Under unphysical expansion shock condition, the numerical dissipation of AUSMPW+ does not become zero due to the additional terms in Eq. (43). From the physical point of view, AUSMPW or Roe's FDS allow an expansion shock solution since they violate the entropy condition. In contrast, AUSMPW+ never allows this situation, which is proved in the following.

Two solutions can be considered that satisfy the inviscid governing equations across a shock discontinuity. In case of $u_L, u_R > 0$,

$$\begin{aligned} &M_L > 1 > M_R > 0, \quad \text{if } p_R > p_L \text{ (compression shock)},\\ &0 < M_L < 1 < M_R, \quad \text{if } p_L > p_R \text{ (expansion shock)}. \end{aligned} \tag{44}$$

The entropy variation across a shock discontinuity are given as

$$\begin{aligned} \Delta s = s_R - s_L &= c_p \ln\left(\frac{T_R}{T_L}\right) - R\ln\left(\frac{p_R}{p_L}\right)\\ &= c_p \ln\left[1+\frac{2\gamma}{\gamma+1}\left(M_L^2-1\right)\right]\left[\frac{2+(\gamma-1)M_L^2}{(\gamma+1)M_L^2}\right] - R\ln\left[1+\frac{2\gamma}{\gamma+1}\left(M_L^2-1\right)\right]. \end{aligned} \tag{45}$$

Then, the entropy variation of Eq. (45) exhibits

$$\begin{aligned} &\Delta s > 0, \quad \text{if } M_L > 1 \text{ (compression shock)},\\ &\Delta s = 0, \quad \text{if } M_L = 1 \text{ (expansion fan, acoustic waves)},\\ &\Delta s < 0, \quad \text{if } M_L < 1 \text{ (expansion shock)}. \end{aligned} \tag{46}$$

Thus it is easily known from Eq. (44) to Eq. (46) that the entropy variation is positive for a compression shock and negative for an expansion shock. Also, the Prandtl relation

$$\frac{u_L}{c^*} \times \frac{u_R}{c^*} = M_L^* M_R^* = 1, \tag{47}$$

where $c^* = \sqrt{2\,(\gamma-1)\,/\,(\gamma+1)\,H_{L\,or\,R}}$ is the critical speed of sound, is satisfied.

From Eqs. (44) and (47), it can be shown that the following properties exist across a shock discontinuity:

$$\begin{aligned} &M^* > 1 \Rightarrow M > 1,\\ &M^* = 1 \Rightarrow M = 1,\\ &M^* < 1 \Rightarrow M < 1. \end{aligned} \tag{48}$$

For an expansion shock, the left and right side of Mach numbers across the shock discontinuity satisfy the condition $0 < M_L^* < 1 < M_R^*$, and the following result can be obtained.

THEOREM (ENTROPY CONDITION OF AUSMPW+). *With the numerical speed of sound defined at a cell interface, Eq.* (30), *the numerical flux function of AUSMPW+ scheme, Eq.* (24), *recognizes an expansion shock and excludes it by the action of the numerical dissipation, Eq.* (43).

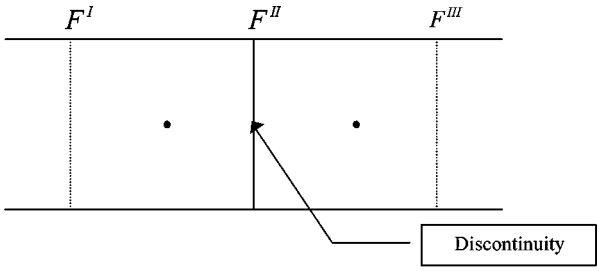

FIG. 3. Fluxes across cell interfaces around an expansion shock discontinuity.

For the initial condition as in Fig. 3, the time evolution of the expansion shock is examined by using AUSMPW and AUSMPW+ schemes.

For AUSMPW, the speed of sound at a cell interface is given as

$$\begin{aligned} c_L = c^*, \quad c_R = \frac{c^{*2}}{|u_R|} = \frac{c^*}{M_R^*}, \\ c_{\frac{1}{2}} = \min(c_L, c_R) = \frac{c^{*2}}{|u_R|}. \end{aligned} \tag{49}$$

And the left and right side Mach numbers are

$$M_L = \frac{u_L|u_R|}{c^{*2}} = M_L^* M_R^* = 1, \quad M_R = \frac{u_R|u_R|}{c^{*2}} = M_R^{*2} > 1. \tag{50}$$

Then, the flux vector at each cell interface becomes

$$\boldsymbol{F} = M_L^+ c_{\frac{1}{2}} \boldsymbol{\Phi}_L + M_R^- c_{\frac{1}{2}} \boldsymbol{\Phi}_R + P_L^+ \boldsymbol{P}_L + P_R^- \boldsymbol{P}_R. \tag{51}$$

From Eq. (51) and the consistency of AUSMPW,

$$\begin{aligned} \boldsymbol{F}^I &= u_L \boldsymbol{\Phi}_L + \boldsymbol{P}_L, \\ \boldsymbol{F}^{II} &= u_L \boldsymbol{\Phi}_L + \boldsymbol{P}_L, \\ \boldsymbol{F}^{III} &= u_R \boldsymbol{\Phi}_R + \boldsymbol{P}_R. \end{aligned} \tag{52}$$

Since $u_L \boldsymbol{\Phi}_L + \boldsymbol{P}_L$ is equal to $u_R \boldsymbol{\Phi}_R + \boldsymbol{P}_R$ across the expansion shock, the conservative vector does not change during the time evolution:

$$\begin{aligned} \boldsymbol{Q}_L^{n+1} = \boldsymbol{Q}_L^n - (\boldsymbol{F}^{II} - \boldsymbol{F}^I) = \boldsymbol{Q}_L^n, \\ \boldsymbol{Q}_R^{n+1} = \boldsymbol{Q}_R^n - (\boldsymbol{F}^{III} - \boldsymbol{F}^{II}) = \boldsymbol{Q}_R^n, \\ \Delta s^{n+1} = \Delta s^n < 0. \end{aligned} \tag{53}$$

Thus the entropy variation keeps its initial value and the expansion shock maintains its initial state. A similar result can be obtained for AUSM, AUSM+, and Roe's FDS.

On the other hand, the speed of sound of AUSMPW+ at a cell interface is given as

$$\begin{aligned} c_L = c^*, \quad c_R = \frac{c^{*2}}{|u_R|} = \frac{c^*}{M_R^*}, \\ c_{\frac{1}{2}} = c_L = c^*. \end{aligned} \tag{54}$$

The left and right side Mach numbers can then be expressed as

$$M_L = \frac{u_L}{c^*} = M_L^* < 1, \quad M_R = \frac{u_R}{c^*} = M_R^* > 1. \tag{55}$$

Thus, the flux vector at each cell interface is given by

$$\boldsymbol{F} = M_L^+ c_{\frac{1}{2}} \boldsymbol{\Phi}_L + M_R^- c_{\frac{1}{2}} \boldsymbol{\Phi}_R + P_L^+ \boldsymbol{P}_L + P_R^- \boldsymbol{P}_R, \tag{56}$$

and the flux vectors in Fig. 3 are

$$\begin{aligned} \boldsymbol{F}^I &= u_L \boldsymbol{\Phi}_L + \boldsymbol{P}_L, \\ \boldsymbol{F}^{II} &= M_L^+ c^* \boldsymbol{\Phi}_L + P_L^+ \boldsymbol{P}_L, \\ \boldsymbol{F}^{III} &= u_R \boldsymbol{\Phi}_R + \boldsymbol{P}_R. \end{aligned} \tag{57}$$

The conservative vector at $t + \Delta t$ may be expressed explicitly as

$$\begin{aligned} \boldsymbol{Q}_L^{n+1} &= \boldsymbol{Q}_L^n - \Delta t (\boldsymbol{F}^{II} - \boldsymbol{F}^I)^n \\ &= \boldsymbol{Q}_L^n + \Delta t [(M_L - M_L^+) c^* \boldsymbol{\Phi}_L + (1 - P_L^+) \boldsymbol{P}_L]^n \\ &= \boldsymbol{Q}_L^n + \Delta t \left[-\frac{1}{4} \left(\frac{u_L}{c^*} - 1 \right)^2 c^* \boldsymbol{\Phi}_L + \frac{1}{4} \left(\frac{u_L}{c^*} - 1 \right)^2 \left(2 + \frac{u_L}{c^*} \right) \boldsymbol{P}_L \right]^n, \end{aligned} \tag{58}$$

and each component of $\boldsymbol{Q}$ at $t + \Delta t$ is

$$Q_1^{n+1} = (1 + C_1) Q_1^n, \tag{59}$$

$$Q_2^{n+1} = \left(1 + C_1 + \frac{C_2 p_L^n}{Q_2^n} \right) Q_2^n, \tag{60}$$

$$Q_3^{n+1} = \left(Q_3^n + C_1 Q_3^n + C_1 p_L^n \right) = \left(1 + C_1 + \frac{C_1 p_L^n}{Q_3^n} \right) Q_3^n. \tag{61}$$

Here, $C_1 = -\frac{1}{4}(M_L^n - 1)^2 c^* \Delta t$ is negative and $C_2 = \frac{1}{4}(M_L^n - 1)^2 (2 + M_L^n) \Delta t$ is positive under the expansion shock condition of Eq. (55).

Now, for the initial values of positive mass (Q_1^n), momentum (Q_2^n), energy (Q_3^n), and pressure (p^n), one must find a time step, Δt, which guarantees positive values of ($\mathbf{Q}$, p) at $t + \Delta t$. From Eqs. (59)–(61) and C_1, C_2, it can be observed that

- Q_1^{n+1} is positive for

$$0 < \Delta t_1 < \frac{4}{\left(M_L^n - 1 \right)^2 c^*},$$

- Q_2^{n+1} is always positive,
- Q_3^{n+1} is positive for

$$0 < \Delta t_2 < 2 \frac{4}{\left(M_L^n - 1 \right)^2 c^* \left(1 + \frac{p_L^n}{Q_3^n} \right)}. \tag{62}$$

After some algebra, it also can be seen for pressure at $t + \Delta t$ that

$$\begin{aligned} p_L^{n+1} &= (\gamma-1)\left(Q_3^{n+1} - 0.5\frac{\left(Q_2^{n+1}\right)^2}{Q_1^{n+1}}\right) \\ &= (\gamma-1)\left[\frac{(1+C_1)}{(\gamma-1)}p_L^n + C_1 p_L^n - C_2\frac{Q_2^n}{Q_1^n}p_L^n - 0.5\frac{C_2^2\left(p_L^n\right)^2}{(1+C_1)\,Q_1^n}\right] \\ &> (\gamma-1)\left[\frac{(1+C_1)}{(\gamma-1)}p_L^n + C_1 p_L^n - C_2\frac{Q_2^n}{Q_1^n}p_L^n - 0.5\frac{C_2^2 Q_3^n p_L^n}{(1+C_1)\,Q_1^n}\frac{(1+C_1)}{-C_1}\right] \quad (63) \\ &= (\gamma-1)\,p_L^n\left[\frac{(1+C_1)}{(\gamma-1)} + C_1 - C_2\frac{Q_2^n}{Q_1^n} - 0.5\frac{C_2^2}{-C_1}\frac{Q_3^n}{Q_1^n}\right]. \end{aligned}$$

Thus, as a sufficient condition to guarantee positive pressure at $t + \Delta t$ it is required that

$$\begin{aligned} &\left[\frac{(1+C_1)}{(\gamma-1)} + C_1 - C_2\frac{Q_2^n}{Q_1^n} - 0.5\frac{C_2^2}{-C_1}\frac{Q_3^n}{Q_1^n}\right] \\ &= \frac{1}{(\gamma-1)} - \frac{1}{4}\left(M_L^n - 1\right)^2\left[\frac{\gamma}{(\gamma-1)}c^* + u_L^n\left(2 + M_L^n\right) + 0.5e_{t,L}^n\frac{\left(2+M_L^n\right)^2}{c^*}\right]\Delta t > 0. \end{aligned}$$

Since the term

$$\frac{1}{4}\left(M_L^n - 1\right)^2\left[\frac{\gamma}{(\gamma-1)}c^* + u_L^n\left(2 + M_L^n\right) + 0.5e_{t,L}^n\frac{\left(2+M_L^n\right)^2}{c^*}\right]\Delta t$$

is always positive, one obtains

$$0 < \Delta t_3 < \frac{1}{(\gamma-1)\,\frac{1}{4}\left(M_L^n - 1\right)^2\left[\frac{\gamma}{(\gamma-1)}c^* + u_L^n\left(2 + M_L^n\right) + 0.5e_{t,L}^n\frac{\left(2+M_L^n\right)^2}{c^*}\right]\Delta t}. \quad (64)$$

Therefore, the time step Δt for positive values of $(\boldsymbol{Q}^{n+1},\ p^{n+1})$ is given by

$$0 < \Delta t < \min\{\Delta t_1,\ \Delta t_2,\ \Delta t_3\}. \quad (65)$$

Now, the velocity and total energy variation can be obtained from Eqs. (59)–(61), and Eq. (56) as

$$u_L^{n+1} - u_L^n = \frac{\Delta t\left[\frac{1}{4}\left(\frac{u_L}{c^*} - 1\right)^2\left(2 + \frac{u_L}{c^*}\right)p_L\right]^n}{\rho_L^{n+1}} > 0, \quad (66)$$

$$e_{t,L}^{n+1} - e_{t,L}^n = \frac{-\Delta t\left[\frac{1}{4}\left(\frac{u_L}{c^*} - 1\right)^2 c^* p_L\right]^n}{\rho_L^{n+1}} < 0. \quad (67)$$

Notice that the velocity in front of the expansion shock increases as the time step evolves while the total energy decreases. Thus, the Mach number on the left side increases since

$$M_L^{n+1} = \left.\frac{u_L}{\sqrt{(\gamma-1)\left(e_{t,L} - 0.5u_L^2\right)}}\right|^{n+1}, \quad (68)$$

and the entropy variation across the expansion shock is gradually decreased from Eq. (46),

$$\Delta s^n < \Delta s^{n+1} < 0. \tag{69}$$

From Eqs. (55) and (68), we have a monotonically increasing bounded sequence $\{M_L^n\}$, and it should converge to 1. Otherwise, there exists a positive number δ such that $1-\delta$ is a limit of $\{M_L^n\}$. Then, from Eqs. (47) and (55), $M_L = 1-\delta$ and $M_R = 1/(1-\delta)$, which produces M_L^n greater than $1-\delta$ through the process of Eqs. (54)–(68). This is a contradiction to the fact that $1-\delta$ is a limit of the monotonically increasing sequence $\{M_L^n\}$. As a result, we have $M_L = M_R = 1$, which means that the initial expansion shock profile is eliminated as time step evolves by the action of the numerical dissipation, Eq. (43).

Numerical results for the entropy condition of AUSMPW+ will be presented in Section 6.1.4.

4.1.4. *Effect of the Speed of Sound to Numerical Dissipation*

AUSM-type schemes are influenced considerably by the choice of the speed of sound at a cell interface. Capability of a shock capturing capability is critically dependent on the choice of the speed of sound. For $m_{1/2} > 0$, the numerical dissipation of convective terms in AUSMPW+ can be expressed as the function of $c_{1/2}$ as

$$\boldsymbol{D} = -\frac{1}{2}(U_L\boldsymbol{\Phi}_L + U_R\boldsymbol{\Phi}_R) + \bar{M}_L^+ c_{\frac{1}{2}}\boldsymbol{\Phi}_L + \bar{M}_R^- c_{\frac{1}{2}}\boldsymbol{\Phi}_R. \tag{70}$$

(i) For $M_L > 1$ and $M_R > 1 (M_L^+ = U_L/c_{1/2}$ and $M_R^- = 0)$

$$\boldsymbol{D} = -\frac{1}{2}(U_R\boldsymbol{\Phi}_R - U_L\boldsymbol{\Phi}_L). \tag{71}$$

(ii) For $M_L > 1$ and $0 < M_R < 1$ $(M_L^+ = U_L/c_{1/2}$ and $M_R^- = -0.25(M_R-1)^2)$

$$\boldsymbol{D} = -\frac{1}{2}(U_R\boldsymbol{\Phi}_R - U_L\boldsymbol{\Phi}_L) - \frac{1}{4}\left(U_R - c_{\frac{1}{2}}\right)^2\frac{\boldsymbol{\Phi}_R}{c_{\frac{1}{2}}}. \tag{72}$$

(iii) For $0 < M_L < 1$ and $0 < M_R < 1$ $(M_L^+ = 0.25(M_L+1)^2$ and $M_R^- = -0.25(M_R-1)^2)$

$$\boldsymbol{D} = -\frac{1}{2}(U_L\boldsymbol{\Phi}_L + U_R\boldsymbol{\Phi}_R) - \frac{1}{4}\left(U_R - c_{\frac{1}{2}}\right)^2\frac{\boldsymbol{\Phi}_R}{c_{\frac{1}{2}}} + \frac{1}{4}\left(U_L + c_{\frac{1}{2}}\right)^2\frac{\boldsymbol{\Phi}_L}{c_{\frac{1}{2}}}. \tag{73}$$

As shown in Eq. (71), the numerical dissipation in supersonic regions is not affected by the choice of the speed of sound. In the transition regions from supersonic to subsonic as in Eq. (72), the numerical dissipation term increases as the speed of sound increases. In subsonic regions as in Eq. (73), it increases as the speed of sound increases in expansion regions ($M_L < M_R$), and it decreases in compression regions ($M_L > M_R$). Since the newly defined speed of sound based on Eq. (30) is always smaller than that of Eq. (11), it may provide more accurate numerical dissipation to capture a shock discontinuity. From the results of test cases presented in Section 6, it is noted that the actual improvement is

significant when the angle difference between a cell interface and a shock discontinuity is small, though its effect may be reduced in case of a large angle difference.

In the boundary layer region, improvement is hardly noticeable since the portion of the numerical dissipation enhanced by the proper choice of the speed of sound is very small compared to the order of the whole numerical dissipation.

4.2. Mechanism to Remove Numerical Oscillations

The fluxes of AUSM+ and AUSMPW+ at a cell interface are

$$\boldsymbol{F}_{\frac{1}{2},AUSM+} = \left(M_L^+\big|_{\beta=\frac{1}{8}} + M_R^-\big|_{\beta=\frac{1}{8}}\right)c_{\frac{1}{2}}\boldsymbol{\Phi}_L + \left(P_L^+\big|_{\alpha=\frac{3}{16}}\boldsymbol{P}_L + P_R^-\big|_{\alpha=\frac{3}{16}}\boldsymbol{P}_R\right), \quad (74)$$

$$\begin{aligned}\boldsymbol{F}_{\frac{1}{2},AUSMPW+} &= (M_L^+ + M_R^- \times ((1-w)\cdot(1+f_R) - f_L))c_{\frac{1}{2}}\boldsymbol{\Phi}_L \\ &\quad + (M_R^- \times w\cdot(1+f_R))c_{\frac{1}{2}}\boldsymbol{\Phi}_R + (P_L^+\boldsymbol{P}_L + P_R^-\boldsymbol{P}_R),\end{aligned} \quad (75)$$

if $m_{1/2} \geq 0$. As mentioned earlier, the advection property of AUSM+ yields the oscillations near a wall and behind a shock in non-shock-aligned grids. It can be seen from Eqs. (74) and (75) that AUSMPW+ is the scheme that controls the advection property by the function f and w without compromising the accuracy of AUSM+. Numerically, AUSM+ chooses $\boldsymbol{\Phi}_L$ only, while AUSMPW+ considers $\boldsymbol{\Phi}_L$ and $\boldsymbol{\Phi}_R$ properly via f and w. In a boundary layer close to a wall, AUSMPW+ incorporates the effect of $\boldsymbol{\Phi}_R$ implicitly through function f_R.

The mechanism to remove oscillations can be explained quantitatively as follows: Near a wall, where $M_{L,R} \to 0$, $w \to 0$, $M_L^+ \to 1/4$, $M_R^- \to -1/4$, and $\boldsymbol{\Phi}_L = \boldsymbol{\Phi}_R$, the numerical dissipation values of AUSM+ and AUSMPW+ become

$$\begin{aligned}\boldsymbol{D}_{\frac{1}{2},AUSM+} &= 0, \\ \boldsymbol{D}_{\frac{1}{2},AUSMPW+} &= -\frac{1}{4}(f_R - f_L)c_{\frac{1}{2}}\boldsymbol{\Phi}_L \cong -\frac{1}{4}\frac{(p_R - p_L)}{p_s}c_{\frac{1}{2}}\boldsymbol{\Phi}_L.\end{aligned} \quad (76)$$

Since the Mach number approaches zero asymptotically in this region, the numerical dissipation becomes zero for AUSM+ while it remains $-\frac{1}{4}(\frac{P_R-P_L}{P_S})c_{1/2}\boldsymbol{\Phi}_L$ for AUSMPW+. Thus pressure oscillations are damped out until p_L equals p_R in AUSMPW+. Additional dissipation due to $f_{L,R}$ does not affect the accuracy since $f_{L,R}$ becomes zero once oscillations are eliminated. A similar mechanism can be seen in Roe's FDS and AUSMD where pressure wiggles do not appear. However, Roe's FDS and AUSMD exhibit carbuncle phenomena because of the numerical dissipation term proportional to the pressure difference [18]. AUSMPW+ also has the possibility of instability due to this term. In AUSMPW+, the numerical dissipation due to pressure difference is carefully controlled to eliminate pressure wiggles without carbuncle phenomena, which is explained in detail in the next section.

In the region of shock waves where $w \to 1$, AUSMPW+ explicitly considers $\boldsymbol{\Phi}_L$ and $\boldsymbol{\Phi}_R$ with the same order of magnitude to remove oscillations. In the supersonic region, the advection property of AUSM+ is compatible with the physical phenomena dominated by the hyperbolic governing equations. In order to fully exploit this property, however, grid generation should reflect the position of physical discontinuities such as a shock-aligned grid system. Under these conditions, an accurate solution such as a shock without an intermediate cell can be captured. Otherwise the advection property of AUSM+ produces

excessive or insufficient convective velocity, and as a result, AUSM+ shows oscillations. On the other hand, AUSMPW+ not only maintains the advection property in a shock-aligned grid system but also removes oscillations in case of non-shock-aligned grids due to $M_R^- w(1 + f_R)c_{1/2}\Phi_R$ of Eq. (75). It is essentially the same mechanism as $M_R^- c_R \Phi_R$ in Van Leer's FVS.

4.3. Preservation of the Total Enthalpy

In hypersonic flows, heat transfer at a wall is one of the primary quantities to be predicted accurately. If a numerical scheme does not guarantee the preservation of the total enthalpy, surface heating rate may be underpredicted since it is very sensitive to the total enthalpy. AUSMPW+, like AUSMPW and AUSM+, is designed to preserve the total enthalpy in steady flows. From the mass conservation, AUSMPW+ satisfies the constancy of the total enthalpy in steady flows because the energy flux of AUSMPW+ can be written as

$$f_3^{\pm} = f_1^{\pm} H, \tag{77}$$

where f_1 is the mass flux.

4.4. Consistency

To solve the given governing equations correctly, the numerical scheme satisfies the following condition. As Δt and Δx approaches zero, properties of both cells are equal, and the numerical flux vector should converge to the physical flux vector of the original governing equations. If $\Delta t,\ \Delta x \to 0$, then $\Phi_L = \Phi_R$ and $\mathbf{P}_L = \mathbf{P}_R$. Thus the pressure ratio of both cells are equal to unity, which gives $f_{L,R} = 0$ and $w = 0$. Then, the split flux vector of AUSMPW+ converges to the physical flux vector as follows:

$$\begin{aligned} \boldsymbol{F}_{\frac{1}{2}} &= \bar{M}_L^+ c_{\frac{1}{2}} \Phi_L + \bar{M}_R^- c_{\frac{1}{2}} \Phi_R + (P_L^+ \boldsymbol{P}_L + P_R^- \boldsymbol{P}_R) \\ &= (M_L^+ + M_R^-) c_{\frac{1}{2}} \Phi_{L,R} + (P_L^+ + P_R^-) \boldsymbol{P}_{L,R} \\ &= U\Phi + \boldsymbol{P}. \end{aligned} \tag{78}$$

4.5. Efficiency

Similar to AUSMPW or AUSM+, AUSMPW+ is based on the form of a scalar dissipation. In addition, thanks to the simplified form of f and interpolation functions, AUSMPW+ is more efficient than AUSMPW, which is useful in the computation of nonequilibrium gas or three-dimensional flows. Table I shows the computational efficiency for a calorically perfect gas. The difference between AUSMPW+ and AUSM+ is shown to be negligible.

TABLE I
Comparison of Computational Time

Scheme	AUSMPW+	AUSMPW	AUSM+	Roe's FDS
Time/time$_{\text{AUSMPW+}}$	1.0	1.03	0.99	1.14

4.6. Robustness and Shock Instability

In hypersonic flow computations involving strong shocks and high expansion regions, a robust numerical scheme is particularly desirable. In this respect, the FVS approach is advantageous since some schemes of FVS are conservatively positive under a CFL-like condition [4]. For AUSM+, only the positivity condition for the mass continuity is satisfied [10]. Since AUSMPW+ has almost the same form as AUSM+, except for the region of oscillations, it satisfies the mass positivity condition, but the complete positivity condition for AUSMPW+ has not yet been fully examined. However, various test cases in Section 6 indicate that AUSMPW+ shows a better robustness than AUSM+ in most hypersonic problems.

In Ref. [18], it is conjectured that if the numerical dissipation term involving pressure difference is not zero in the mass flux, a scheme may show even–odd decoupling and carbuncle phenomena. From this point of view, it is possible that AUSMPW+ may exhibit even–odd decoupling and carbuncle phenomena since AUSMPW+ possesses the numerical dissipation term formed by the pressure difference.

In AUSMPW+, the numerical dissipation of mass flux is given by

$$\begin{aligned} D_1 &= -\frac{1}{2}\left[(M_R - 2\bar{M}_R^-)c_{\frac{1}{2}}\rho_R + (M_L - 2\bar{M}_L^-)c_{\frac{1}{2}}\rho_L\right] \\ &= -\frac{1}{2}\left[(M_R^+ - M_R^-)c_{\frac{1}{2}}\rho_R + (M_L^- - M_L^+)c_{\frac{1}{2}}\rho_L\right] \\ &\quad + M_R^- w(1 + f_R)c_{\frac{1}{2}}(\rho_R - \rho_L) + M_R^-(f_R - f_L)c_{\frac{1}{2}}\rho_L, \end{aligned} \tag{79}$$

when $m_{1/2} > 0$, and the term involving the pressure difference is

$$D_1^{(p)} = M_R^-\left(\frac{p_R - p_L}{p_s}\right)c_{\frac{1}{2}}\rho_L$$

if $f = (p/p_s - 1)$. Figure 4 shows the situation that induces even–odd decoupling and carbuncle phenomena. For large convection velocity, $D_1^{(p)}$ is insufficient to induce instability. For small convection velocity such as in the η-direction, however, it becomes enough to trigger the instability.

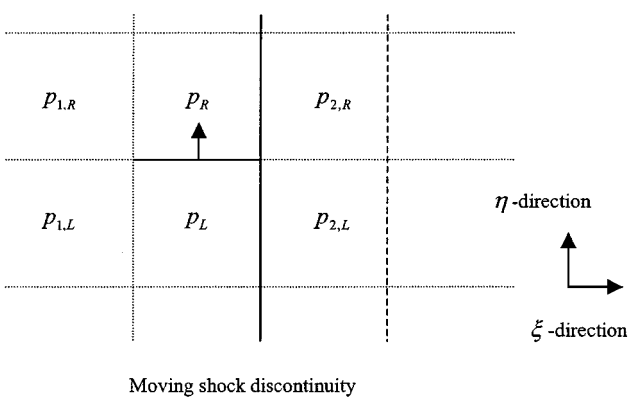

FIG. 4. Pressure distribution around a moving shock discontinuity.

By some external disturbances such as a grid disturbance, the instability by $D_1^{(p)}$ magnifies as shock strength increases. In order to remove this problem actively, it is necessary that the order of magnitude of $D_1^{(p)}$ should be scaled down to the level where the instability is easily damped out by numerical dissipation. This is achieved by augmenting the term that considers transversal pressure ratio to f as

$$f_{L,R} = \left(\frac{p_{L,R}}{p_s} - 1\right)\min\left(1, \frac{\min(p_{1,L}, p_{1,R}, p_{2,L}, p_{2,R})}{\min(p_L, p_R)}\right)^2. \tag{80}$$

Extensive numerical tests indicate that Eq. (80) is sufficient to suppress even–odd decoupling and carbuncle phenomena.

4.7. Extension to Reacting Gases

Like AUSM+, AUSMPW+ defines an advection Mach number and the speed of sound at a cell interface with which convective fluxes are determined. Thus AUSMPW+ can be easily extended to reacting gases. This requires the addition of species densities or vibrational energies of molecules to the flow vector

$$\mathbf{\Phi} = (\rho, \rho u, \rho H, \rho_1, \rho_{2,}, \ldots, \rho_s, \rho_1 e_{vib,1}, \ldots, \rho_s e_{vib,s})^T. \tag{81}$$

For equilibrium and nonequilibrium gases, the speed of sound should take into account the effect of the species variation due to chemical reactions. Thus $c^2 = \gamma p/\rho$ is not valid and is given by a variable specific heat ratio such as $c^2 = \tilde{\gamma}(\tilde{\gamma} - 1)e = \tilde{\gamma} p/\rho$. From the conservation laws and equation of state, the speed of sound satisfying the Prandtl relation can be derived. The conservation laws across a normal shock are

Continuity equation:

$$\rho_L U_L = \rho_R U_R,$$

Momentum equation:

$$p_L + \rho_L U_L^2 = p_R + \rho_R U_R^2, \tag{82}$$

Energy equation:

$$H_L = h_L + \frac{1}{2}U_L^2 = h_R + \frac{1}{2}U_R^2 = H_R.$$

From the above shock relation equations, we can obtain

$$\frac{p_L}{\rho_L U_L} - \frac{p_R}{\rho_R U_R} = (\tilde{\gamma}_L - 1)\frac{e_L}{U_L} - (\tilde{\gamma}_R - 1)\frac{e_R}{U_R} = U_R - U_L, \tag{83}$$

$$\tilde{\gamma}^* e^* + \frac{1}{2}c^{*2} = \left(\frac{1}{\tilde{\gamma}^* - 1} + \frac{1}{2}\right)c^{*2} = \tilde{\gamma}_L e_L + \frac{1}{2}U_L^2, \tag{84}$$

$$\tilde{\gamma}^* e^* + \frac{1}{2}c^{*2} = \left(\frac{1}{\tilde{\gamma}^* - 1} + \frac{1}{2}\right)c^{*2} = \tilde{\gamma}_R e_R + \frac{1}{2}U_R^2, \tag{85}$$

where $\tilde{\gamma}$ is variable specific heat ratio according to the gas reaction, and the superscript * stands for the critical state from the isoenergetic condition as in Eq. (11). Inserting Eqs. (84)

and (85) into Eq. (83), we obtain

$$\left(\frac{1}{\tilde{\gamma}^*-1}+\frac{1}{2}\right)c^{*2}\left(\frac{(\tilde{\gamma}_L-1)/\tilde{\gamma}_L U_R-(\tilde{\gamma}_R-1)/\tilde{\gamma}_R U_L}{U_L U_R}\right)$$
$$+\frac{1}{2}\left((\tilde{\gamma}_R-1)/\tilde{\gamma}_R U_R-(\tilde{\gamma}_L-1)/\tilde{\gamma}_L U_L\right)=U_R-U_L. \tag{86}$$

After defining c_s as in Eq. (32) to satisfy the Prandtl relation

$$c_s^2=U_L U_R, \tag{87}$$

c_s is given as

$$c_s=c^*\left(\left(\frac{\tilde{\gamma}^*+1}{\tilde{\gamma}^*-1}\right)\times\left(\frac{(\tilde{\gamma}_L-1)/\tilde{\gamma}_L U_R-(\tilde{\gamma}_R-1)/\tilde{\gamma}_R U_L}{(\tilde{\gamma}_R+1)/\tilde{\gamma}_R U_R-(\tilde{\gamma}_L+1)/\tilde{\gamma}_L U_L}\right)\right)^{0.5}. \tag{88}$$

Equation (88) is consistent in the sense that it is identical to the critical speed of sound ($c^*=[2(\gamma-1)/(\gamma+1)H]^{1/2}$) when the effect of reacting gas is neglected. In order to capture the oblique shock exactly, Eq. (88) is reformulated as

$$c_s=\left(2H_{normal}\frac{(\tilde{\gamma}_L-1)/\tilde{\gamma}_L U_R-(\tilde{\gamma}_R-1)/\tilde{\gamma}_R U_L}{(\tilde{\gamma}_R+1)/\tilde{\gamma}_R U_R-(\tilde{\gamma}_L+1)/\tilde{\gamma}_L U_L}\right)^{0.5}$$
$$=\left(2H_{normal}\frac{(\tilde{\gamma}_L-1)/\tilde{\gamma}_L \rho_L-(\tilde{\gamma}_R-1)/\tilde{\gamma}_R \rho_R}{(\tilde{\gamma}_R+1)/\tilde{\gamma}_R \rho_L-(\tilde{\gamma}_L+1)/\tilde{\gamma}_L \rho_R}\right)^{0.5}. \tag{89}$$

5. TEMPORAL INTEGRATION

The governing equations are discretized using the backward Euler formula as

$$\left[\frac{\boldsymbol{I}}{J\Delta t}+\delta_\xi^-\hat{\boldsymbol{A}}^+ +\delta_\xi^+\hat{\boldsymbol{A}}^- +\delta_\eta^-\hat{\boldsymbol{B}}^+ +\delta_\eta^+\hat{\boldsymbol{B}}^-\right]^n \Delta\boldsymbol{Q}_{i,j}^n=-\boldsymbol{R}_{i,j}^n,$$
$$\boldsymbol{R}_{i,j}^n=\left[\frac{\partial\hat{\boldsymbol{E}}}{\partial\xi}+\frac{\partial\hat{\boldsymbol{F}}}{\partial\eta}-\left(\frac{\partial\hat{\boldsymbol{E}}_\nu}{\partial\xi}+\frac{\partial\hat{\boldsymbol{F}}_\nu}{\partial\eta}\right)\right]_{i,j}^n, \tag{90}$$

where $\Delta\boldsymbol{Q}_{i,j}^n=\boldsymbol{Q}_{i,j}^{n+1}-\boldsymbol{Q}_{i,j}^n$, $\hat{\boldsymbol{A}}=\partial\hat{\boldsymbol{E}}/\partial\boldsymbol{Q}$ and $\hat{\boldsymbol{B}}=\partial\hat{\boldsymbol{F}}/\partial\boldsymbol{Q}$.

The matrix on the left-hand side of Eq. (90) can be inverted approximately by the Approximate Factorization Alternate Direction Implicit (AF-ADI) or Lower Upper Symmetric Gauss Seidel (LU-SGS) scheme. The AF-ADI scheme is used for the calorically perfect gas and the equilibrium gas since the flux Jacobian can be obtained analytically; in the nonequilibrium gas, the LU-SGS scheme is adopted for the efficient calculation of the flux Jacobian and matrix inversion:

AF-ADI:

$$\left[\frac{\boldsymbol{I}}{J\Delta t}+\delta_\xi^-\hat{\boldsymbol{A}}^+ +\delta_\xi^+\hat{\boldsymbol{A}}^-\right]\Delta\boldsymbol{Q}_{i,j}^{*n}=-\boldsymbol{R}_{i,j}^n,$$
$$\left[\frac{\boldsymbol{I}}{J\Delta t}+\delta_\eta^-\hat{\boldsymbol{B}}^+ +\delta_\eta^+\hat{\boldsymbol{B}}^-\right]\Delta\boldsymbol{Q}_{i,j}^n=\frac{\boldsymbol{I}}{J\Delta t}\Delta\boldsymbol{Q}_{i,j}^{*n}.$$

LU-SGS:

$$\boldsymbol{L}\boldsymbol{D}^{-1}\boldsymbol{U}\Delta\boldsymbol{Q}^n_{i,j} = -\boldsymbol{R}^n_{i,j},$$

$$\boldsymbol{L} = \frac{\boldsymbol{I}}{J\Delta t} + \delta^-_\xi \hat{\boldsymbol{A}}^+ + \delta^-_\eta \hat{\boldsymbol{B}}^+ - \hat{\boldsymbol{A}}^- - \hat{\boldsymbol{B}}^- - \boldsymbol{C},$$

$$\boldsymbol{D} = \frac{\boldsymbol{I}}{J\Delta t} + \hat{\boldsymbol{A}}^+ + \hat{\boldsymbol{B}}^+ - \hat{\boldsymbol{A}}^- - \hat{\boldsymbol{B}}^-,$$

$$\boldsymbol{U} = \frac{\boldsymbol{I}}{J\Delta t} + \delta^+_\xi \hat{\boldsymbol{A}}^- + \delta^+_\eta \hat{\boldsymbol{B}}^- - \hat{\boldsymbol{A}}^+ - \hat{\boldsymbol{B}}^+.$$

Here

$$\hat{\boldsymbol{A}}^\pm = \frac{1}{2}(\hat{\boldsymbol{A}} \pm \kappa\,|\max(\text{eigenvalue}(\hat{\boldsymbol{A}}))|),$$

and $\boldsymbol{C} = \partial \boldsymbol{S}/\partial \boldsymbol{Q}$.

6. NUMERICAL RESULTS OF AUSMPW+

To validate the analysis carried out in Section 4, various numerical computations are performed. The test problems include shock discontinuities, contact discontinuities, shock wave/boundary layer interaction, compressible boundary layer flows, and hypersonic reacting gas flows. Test cases for a calorically perfect gas are presented in Sections 6.1–6.5. Results for equilibrium and nonequilibrium gases are given in Section 6.6.

For boundary conditions, free-stream values are specified as inflow conditions, and extrapolation from the inner computational domain is used for outflow conditions. At a wall, a no-slip condition is specified for velocity, and an adiabatic or constant condition is used for wall temperature. For the nonequilibrium gas, the wall is assumed to be fully catalytic.

6.1. Shock Discontinuities

6.1.1. *Stationary Normal Shock*

For the normal shock condition with a Mach number of 3, initial conditions are given by $(\rho,\ u,\ p)_L = (1,\ 3,\ 0.714)$ and $(\rho,\ u,\ p)_R = (3.857,\ 0.778,\ 7.381)$. CFL is 1.0 and all results are converged to the machine accuracy zero. As shown in Fig. 5, AUSMPW+ and AUSMPW capture the normal shock with one cell interface only. AUSM+ and Roe's FDS also satisfy this property. As proved in Section 4, the functions f and w are not active in shock-aligned grids.

6.1.2. *Stationary Oblique Shock*

Initial conditions are $(\rho,\ u,\ v,\ p)_L = (1,\ 1.5,\ 2.598,\ 0.714)$ and $(\rho,\ u,\ v,\ p)_R = (1.862,\ 0.806,\ 2.598,\ 1.756)$, which produces an oblique shock with a 30 degree shock angle and the Mach number of 3. CFL is 1.0 and all results are converged to the machine accuracy zero. Figures 6 to 8 show the comparison of pressure distributions with three speeds of sound. Case 1 is the speed of sound in Eq. (11) used in AUSM+ and AUSMPW, case 2 is the newly defined speed of sound in Eq. (30), and case 3 is the speed of sound in

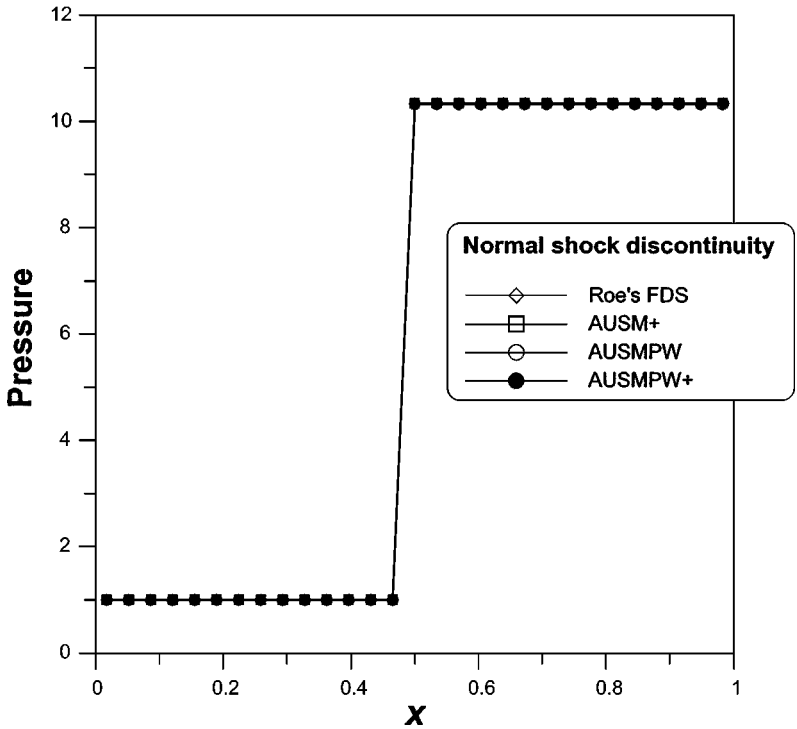

FIG. 5. Pressure distribution of a normal shock.

Eq. (89) for equilibrium flow. Figure 6 shows the accuracy comparison of each scheme with the same speed of sound. Calculation of the discontinuity by AUSMPW+ is more accurate than the other schemes in Fig. 6 since Mach number and pressure splitting functions of AUSMPW+ are less diffusive than the other schemes. Figure 7 shows that AUSMPW+ of case 2 can capture the oblique shock in one cell interface while AUSM+ and AUSMPW produce more than three interior cells in the shock transition layer. Figure 8 shows that AUSMPW+ of case 3 successfully captures the oblique shock through a one cell interface even in an equilibrium reacting gas flow. As in the previous test case, the functions f and w are not active in shock-aligned grids.

6.1.3. *Moving Normal Shock*

The problem of a shock wave propagating through a two-dimensional duct is chosen to examine carbuncle phenomena. Centerline grids are perturbed according to Ref. [6]. The initial conditions are $(\rho,\ u,\ v,\ p)_L = (1,\ 6,\ 0,\ 1)$ and $(\rho,\ u,\ v,\ p)_R = (5.25,\ 0.353,\ 0,\ 40.64)$ to produce a normal shock propagated with a Mach number of 6. CFL is 1.0 and the iteration count is 2000. As in Fig. 9, AUSMPW+, AUSMPW, and AUSM+ do not show carbuncle phenomena.

6.1.4. *Expansion Shock*

The initial conditions are given by $(\rho,\ u,\ p)_L = (1,\ -3,\ 0.714)$ and $(\rho,\ u,\ p)_R = (3.857,\ -0.778,\ 7.381)$ for an expansion shock condition with a Mach number of 3. CFL

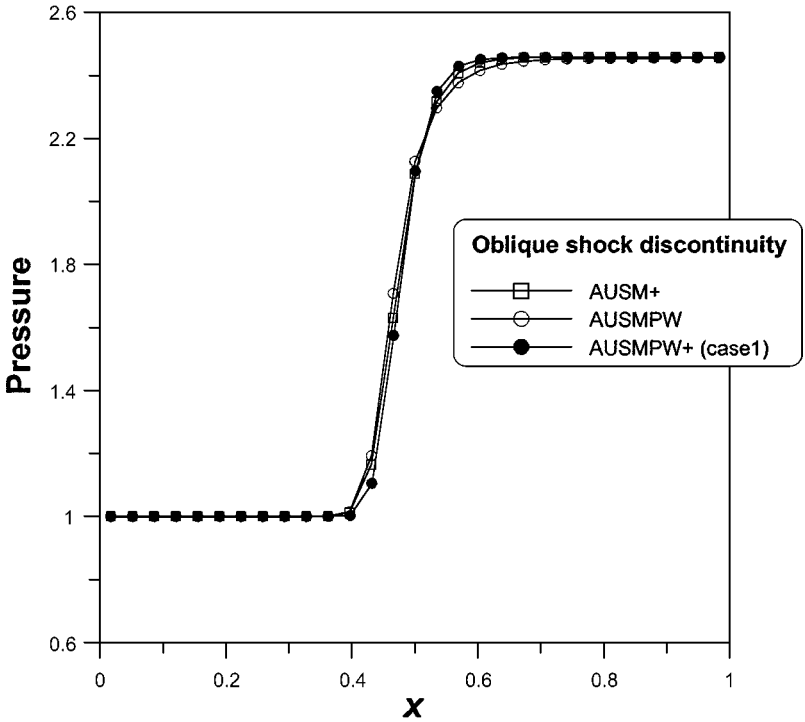

FIG. 6. Pressure distribution of an oblique shock (case 1).

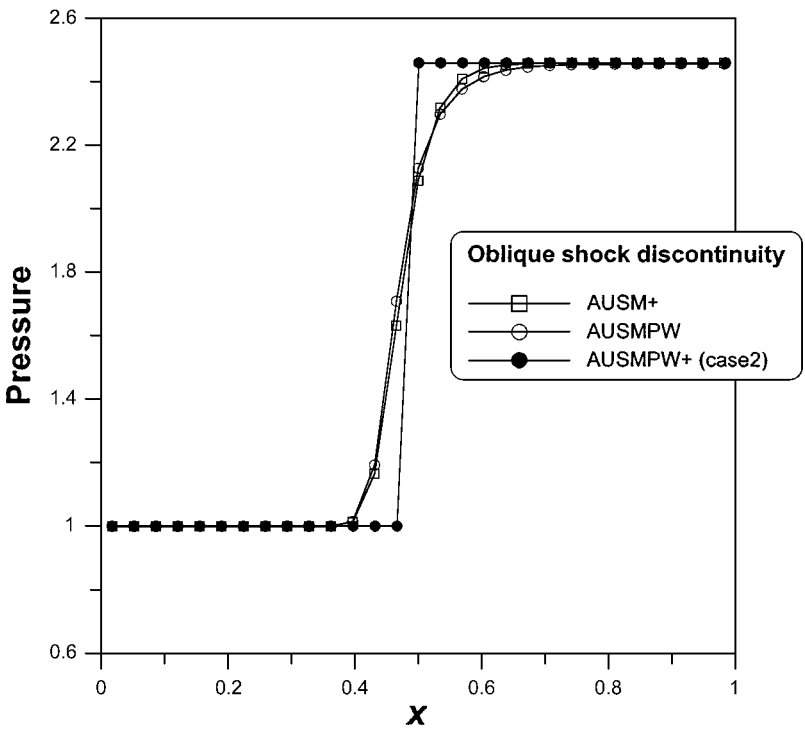

FIG. 7. Pressure distribution of an oblique shock (case 2).

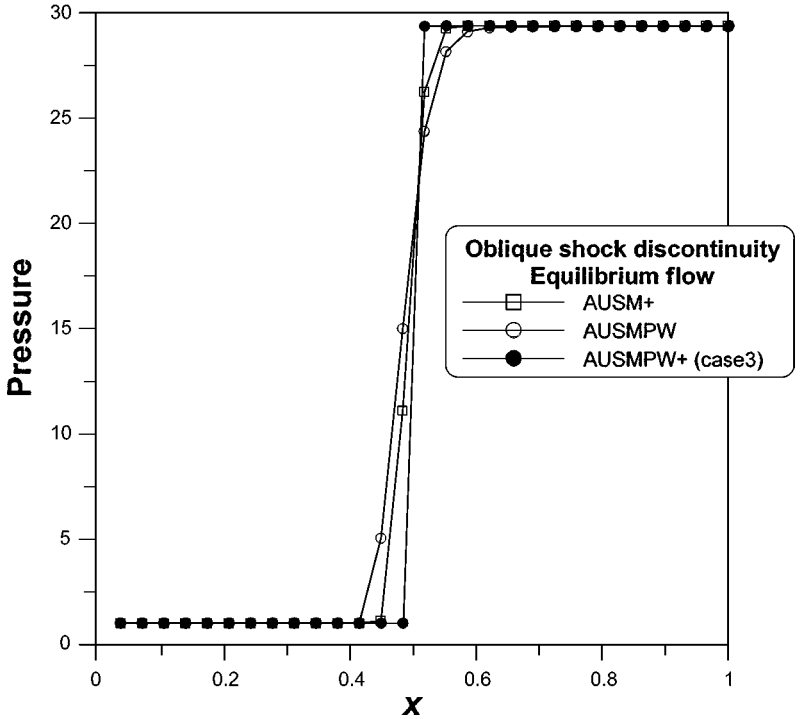

FIG. 8. Pressure distribution of an equilibrium oblique shock (case 3).

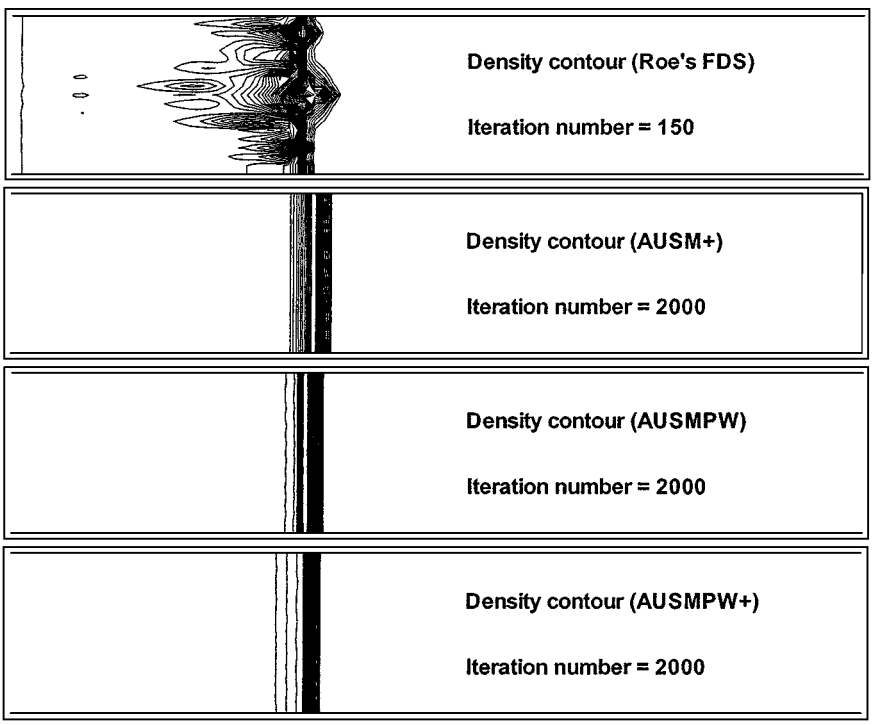

FIG. 9. Moving normal shock with the Mach number of 6.

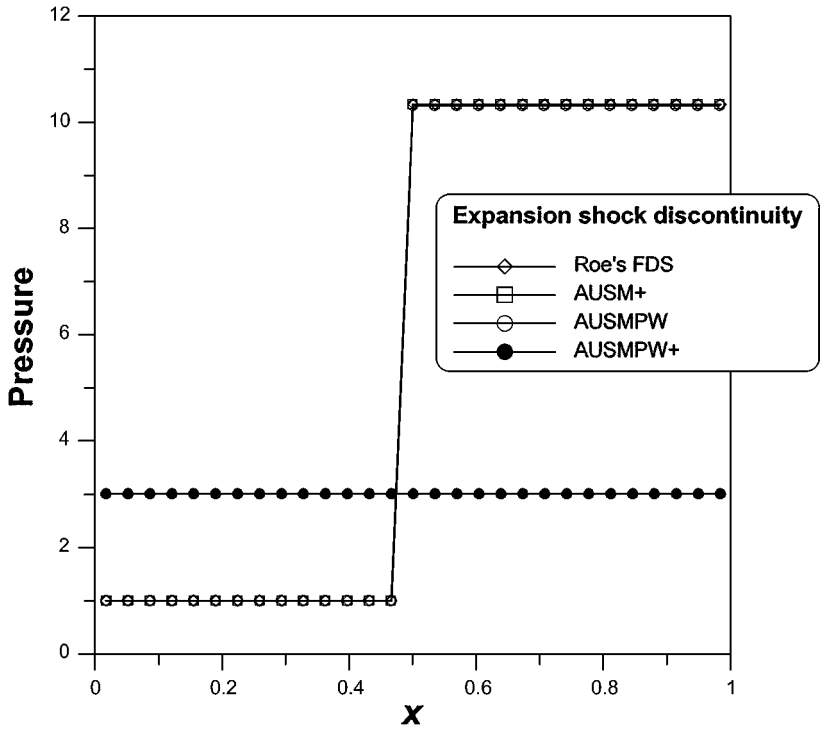

FIG. 10. Pressure distribution under an expansion shock condition.

is 1.0 and all results are converged to the machine accuracy zero. As can be seen in Fig. 10, Roe's FDS without an entropy fix, AUSM+, and AUSMPW admit a physically unacceptable discontinuity. On the other hand, AUSMPW+ with the newly proposed speed of sound eliminates it.

6.2. Contact Discontinuities

6.2.1. *Stationary Contact Discontinuity*

The initial conditions are $(\rho,\ u,\ p)_L = (1,\ 0,\ 1)$ and $(\rho,\ u,\ p)_R = (10,\ 0,\ 1)$ with a CFL number of 1.0. All results are converged to the machine accuracy zero. As in Fig. 11, AUSMPW+ yields a very satisfactory result because the mass flux disappears as the Mach number goes to zero, like AUSM+, AUSMPW, or Roe's FDS. It also confirms that f and w do not compromise accuracy.

6.2.2. *Moving Contact Discontinuity*

The initial conditions are $(\rho,\ u,\ p)_L = (0.125,\ 0.1125,\ 1)$ and $(\rho,\ u,\ p)_R = (10,\ 0.1125,\ 1)$ with a CFL number of 0.7. The iteration count is 500 and the number of grid points is 100. AUSMPW+, AUSMPW, and AUSM+ adopted the speed of sound given in Eq. (11). AUSMPW+ and Roe's FDS without an entropy fix give almost the same results as shown in Fig. 12 but large oscillations in velocity profile can be observed in the case of AUSM+, indicating that the function f in AUSMPW+ plays a crucial role in damping out the oscillations. However, when CFL number becomes 1, both AUSMPW+

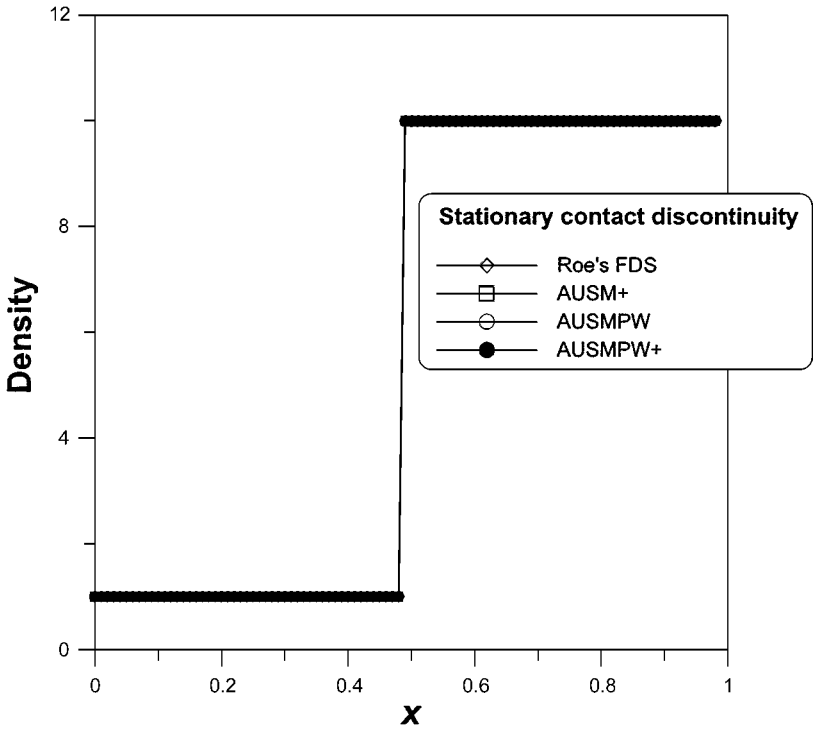

FIG. 11. Density distribution of a stationary contact discontinuity.

and AUSMPW, in contrast to Roe's FDS, show velocity oscillations. In view of stability, the numerical dissipation by the convective term in the slowly moving contact discontinuity problem is so small that the numerical dissipation due to the pressure splitting function becomes important. When convective velocity is large, however, there is no problem in solving this test case. Thus, AUSM-type schemes with a pressure splitting function in Eq. (10) seem to be insufficient to prevent oscillations. If α becomes 0, the pressure splitting function is almost the same as that of Roe's FDS, and AUSM-type schemes also show the same level of robustness as Roe's FDS.

6.3. Hypersonic Inviscid Flow around a Cylinder

The free-stream conditions are

- calorically perfect gas,
- $M_\infty = 10.0$.

The conditions for the computation are

- time integration : CFL = 1.0, LU-SGS,
- spatial discretization : AUSMPW+, AUSM+; the number of grid points = 9394 nodes (see Fig. 13),
- boundary condition: slip condition.

To check the sensitivity of a scheme to grid topology, an unstructured mesh is used. As in Fig. 14, AUSM+ yields noticeable oscillations near the stagnation region while the oscillatory behavior is effectively eliminated in AUSMPW+ by the pressure-based weight

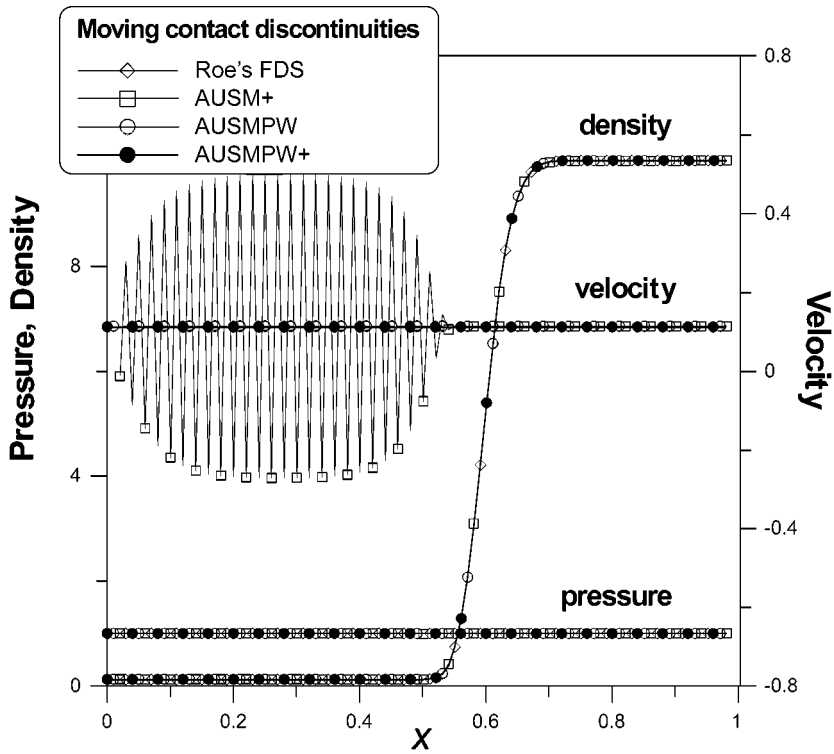

FIG. 12. Pressure, density, and velocity distributions of a slowly moving contact discontinuity.

function w. This can be seen more clearly in Fig. 15, which shows the distribution of surface pressure coefficients for AUSM+ and AUSMPW+. In AUSM+, the overshoot in the stagnation region and asymmetric pressure distribution in the expansion region can be observed. The error due to oscillations around the normal shock and stagnation region is propagated along the flow and produces the asymmetric pressure distribution in the expansion region. Figure 16 indicates that the oscillatory behavior also produces an adverse effect in convergence behavior.

6.4. Shock Wave/Laminar Boundary Layer Interaction

The free-stream conditions are

- calorically perfect gas,
- $M_\infty = 2.0$,
- $Re = 2.96 \times 10^5$,
- $Pr = 0.72$,
- $\theta_{impinging\ shock\ angle} = 32.585^\circ$.

The conditions for the computation are

- time integration : CFL $= 3.0$, AF-ADI,
- spatial discretization : AUSMPW+, AUSM+, Roe FDS; third-order MUSCL without limiter ($\kappa = 1/3$); the number of grid point $= 55 \times 60$ (see Fig. 17),
- boundary condition : adiabatic wall condition.

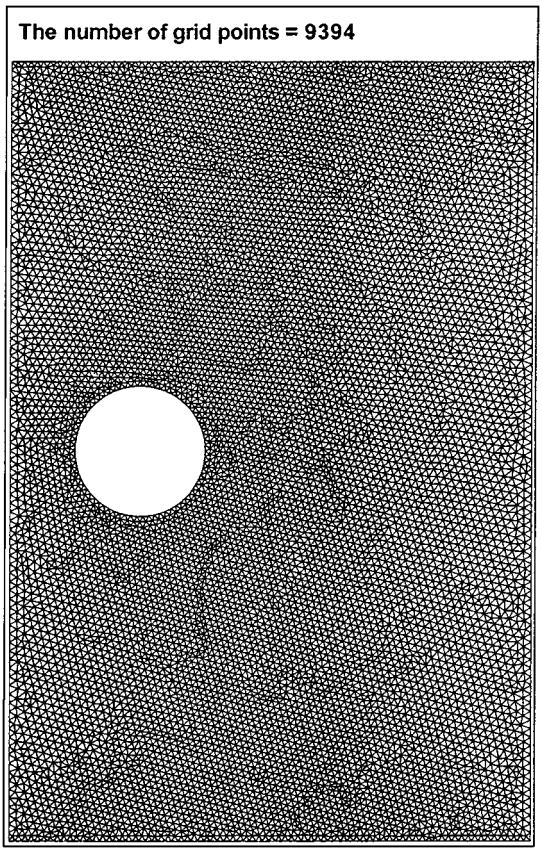

FIG. 13. Unstructured grids around a cylinder.

Figure 18 shows that the skin friction coefficient of AUSMPW+ is in a good agreement with other numerical results and experimental data, indicating the capability of AUSMPW+ to compute viscous flows involving shock waves. It is also noticed that f and w do not compromise accuracy in viscous calculations compared with results of AUSM+ and Roe's

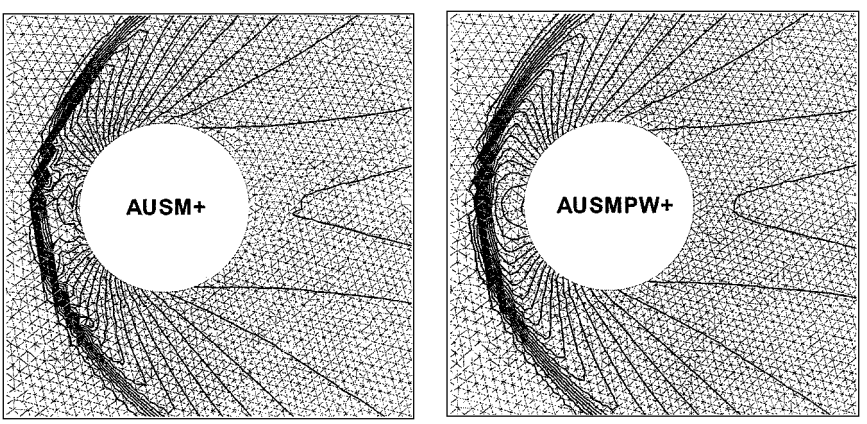

FIG. 14. Comparison of pressure contours.

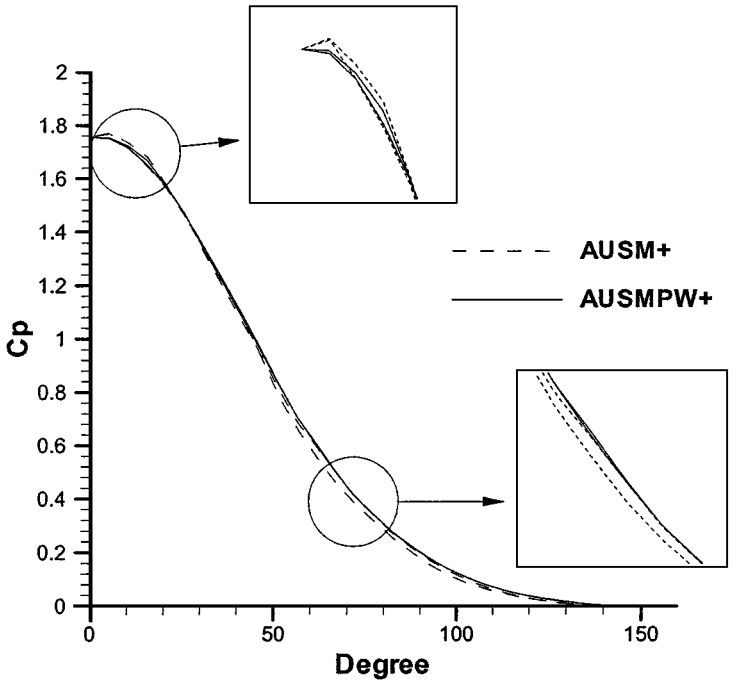

FIG. 15. Surface pressure coefficient.

FDS. Figure 19 shows the convergent behavior of AUSMPW+, AUSM+, and Roe's FDS. The error history of AUSMPW+ is similar to those of AUSM+ or Roe's FDS. Although numerical oscillations near a wall are also observed for AUSM+, it does not interfere with convergence characteristics since shock strength is relatively weak.

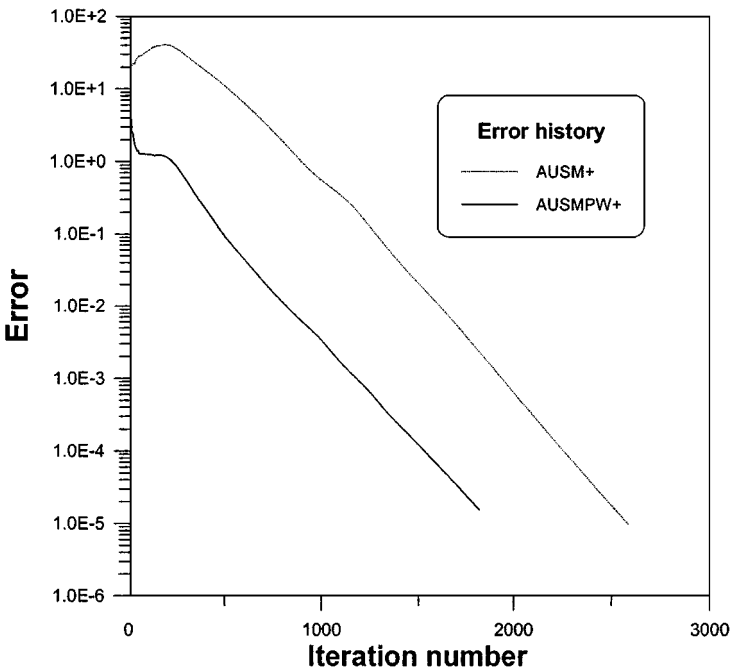

FIG. 16. Convergence history of the cylinder problem.

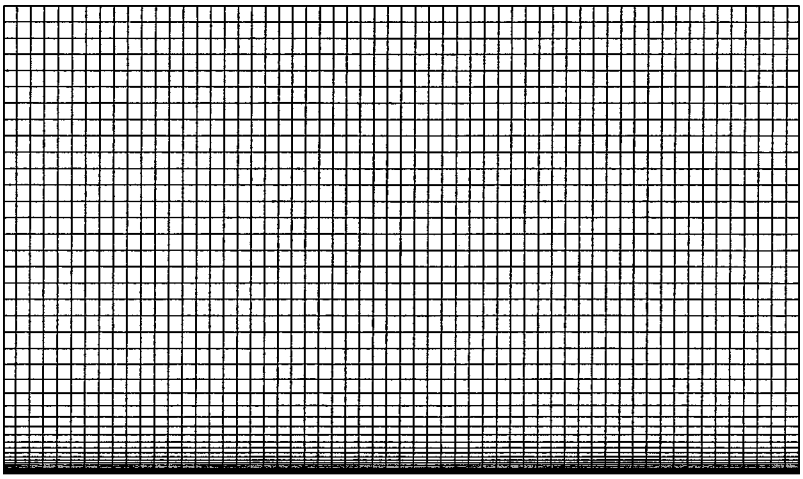

FIG. 17. Grid system for the shock wave/boundary layer interaction problem. The number of grid points = 55×60.

6.5. Boundary Layer over a Flat Plate

The free-stream conditions for a laminar boundary layer over a flat plate are

- calorically perfect gas,
- $M_\infty = 0.2$,
- $Re = 1.0 \times 10^5$.

The conditions for the computation are

- time integration : CFL = 1.0, AF-ADI,

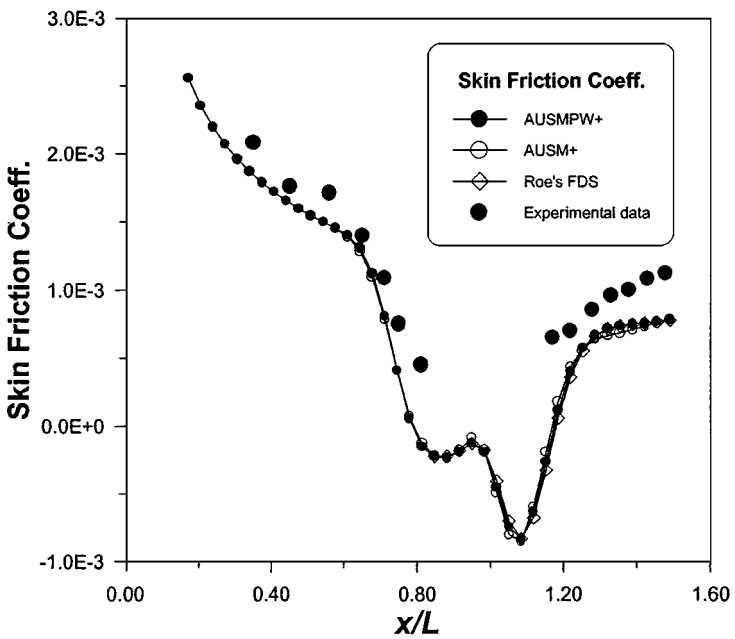

FIG. 18. Skin friction coefficient of the shock wave/boundary layer interaction problem.

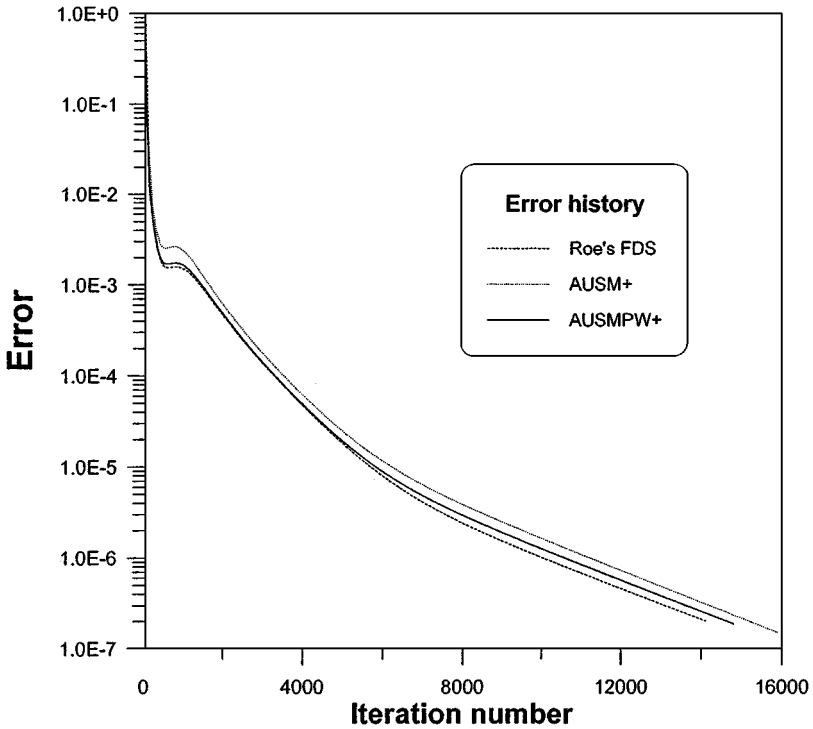

FIG. 19. Convergence history of the shock wave/boundary layer interaction problem.

- spatial discretization : AUSMPW+, AUSM+, and Roe's FDS; third-order MUSCL without limiter ($\kappa = 1/3$); the number of grid point $= 128 \times 64$ (see Fig. 20),
- boundary condition : adiabatic wall condition.

Figures 21 and 22 show comparison of the velocity profiles of each scheme with the Blasius solutions. According to Ref. [19], 32 cells are equally distributed inside the boundary layer. Like AUSM+ and Roe's FDS, AUSMPW+ yields an excellent agreement with the u and v profiles of the Blasius solution. It confirms again that f and w do not compromise accuracy. Figure 23 shows the error histories of AUSMPW+, AUSM+, and Roe's FDS, confirming again the convergence characteristics of AUSMPW+.

6.6. Equilibrium and Nonequilibrium Flows around a Cylinder

The free-stream conditions are

- equilibrium and nonequilibrium gas,
- $M_\infty = 15$,
- $p_\infty = 663.41\,\mathrm{N/m^2}$,
- $\rho_\infty = 9.8874 \times 10^{-3}\,\mathrm{kg/m^3}$,
- $\mu_\infty = 1.514 \times 10^{-5}\,\mathrm{kg/m \cdot s^2}$,
- $T_\infty = 233.75\,\mathrm{K}$,
- $T_{wall} = 1168.7\,\mathrm{K}$,
- $Re = 2.0 \times 10^5$.

The conditions for the computation are

- time integration : CFL $= 0.5$, LU-SGS,

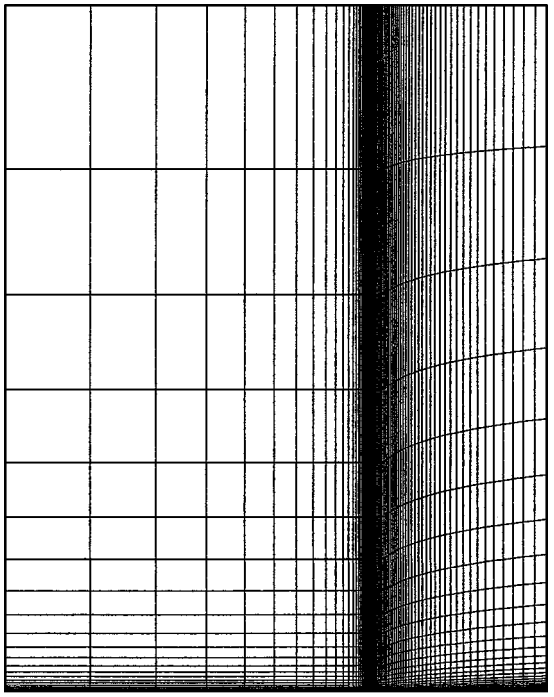

FIG. 20. Grid system for the flat plate. The number of grid points = 128 × 64.

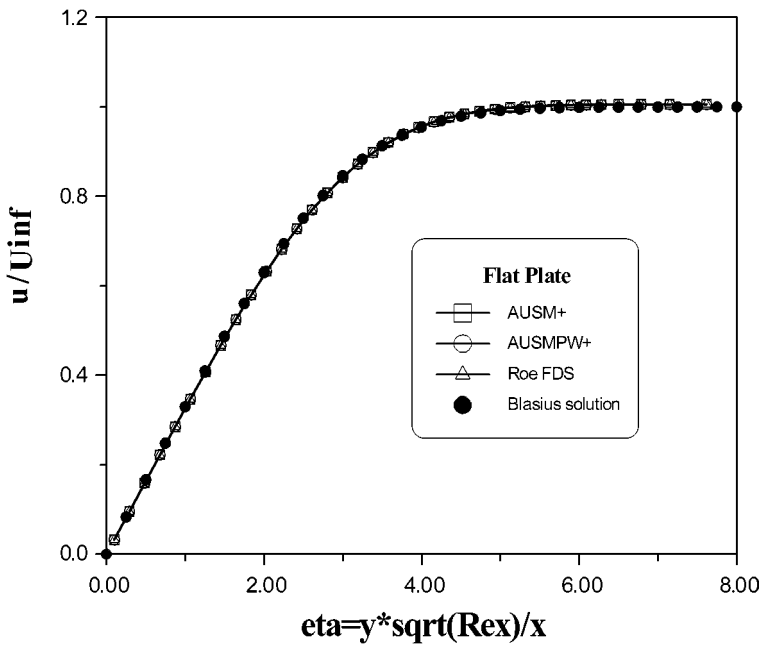

FIG. 21. *u* profile.

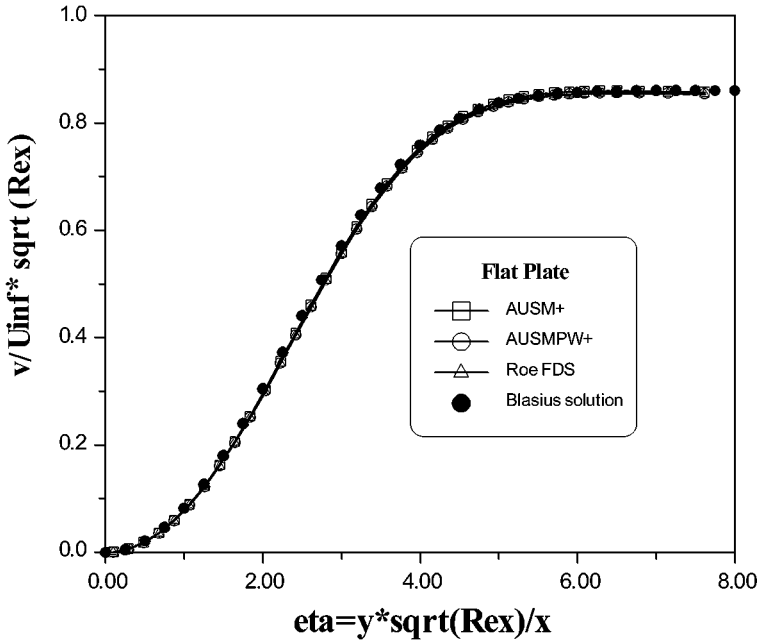

FIG. 22. *v* profile.

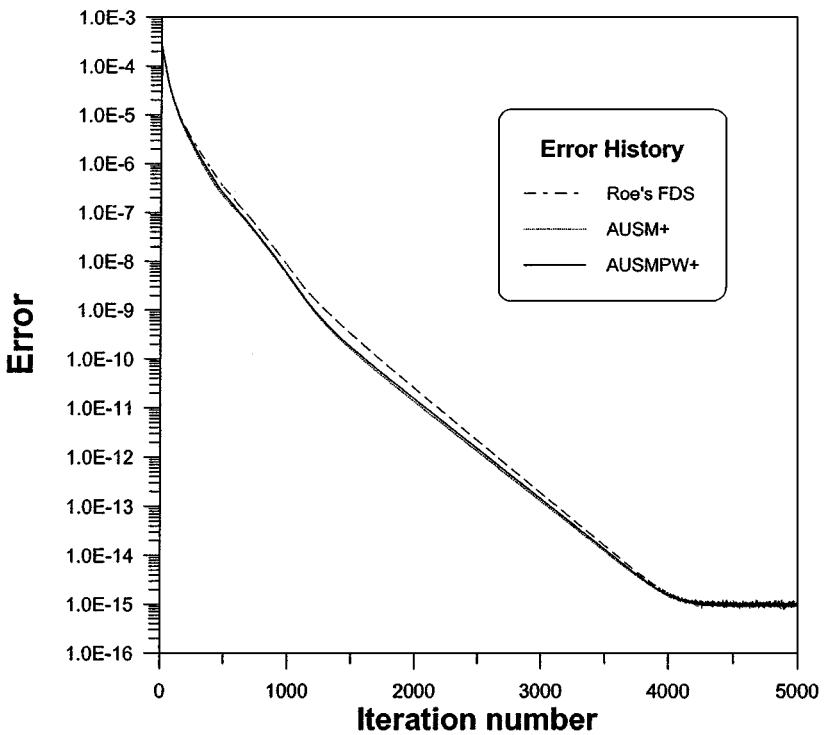

FIG. 23. Convergence history of the flat plate problem.

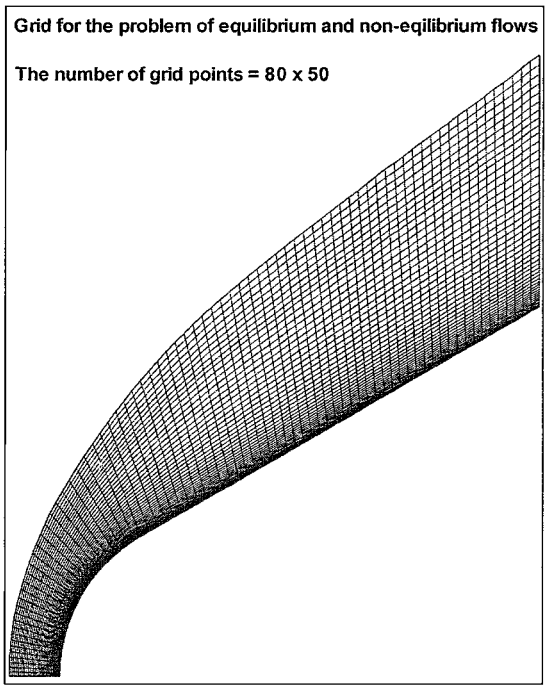

FIG. 24. Grid system for the blunt wedge.

- spatial discretization : AUSMPW+, AUSM+; third-order MUSCL with minmod limiter ($\beta = 1, \kappa = 1/3$); the number of grid point $= 80 \times 55$ (see Fig. 24),
- boundary condition: constant temperature wall (fully catalytic wall).

Figures 25 to 29 are the results of AUSMPW+ and AUSM+ applied to equilibrium and nonequilibrium flows. The result of nonequilibrium flow is obtained by the four-temperature

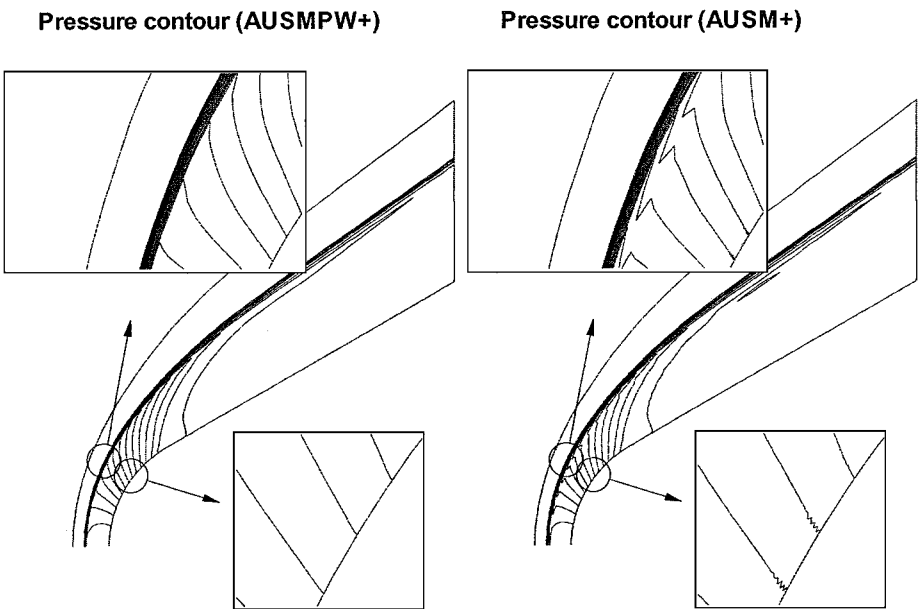

FIG. 25. Comparison of pressure distributions (AUSMPW+, AUSM+) around an equilibrium blunt wedge.

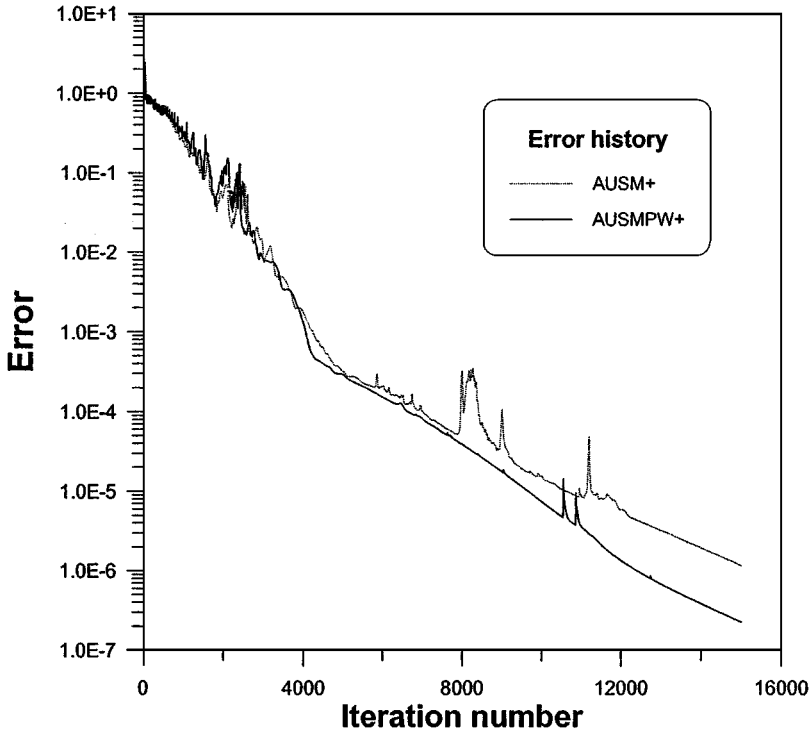

FIG. 26. Convergence history of the equilibrium blunt-wedge problem.

model. Although the two-temperature model is sufficient to obtain accurate results in most hypersonic flow problems, the four-temperature model is adopted in the present work to test the robustness of AUSMPW+ in nonequilibrium flows. Since structured grids are much more aligned than unstructured grids, the oscillatory phenomena of AUSM+ are substantially

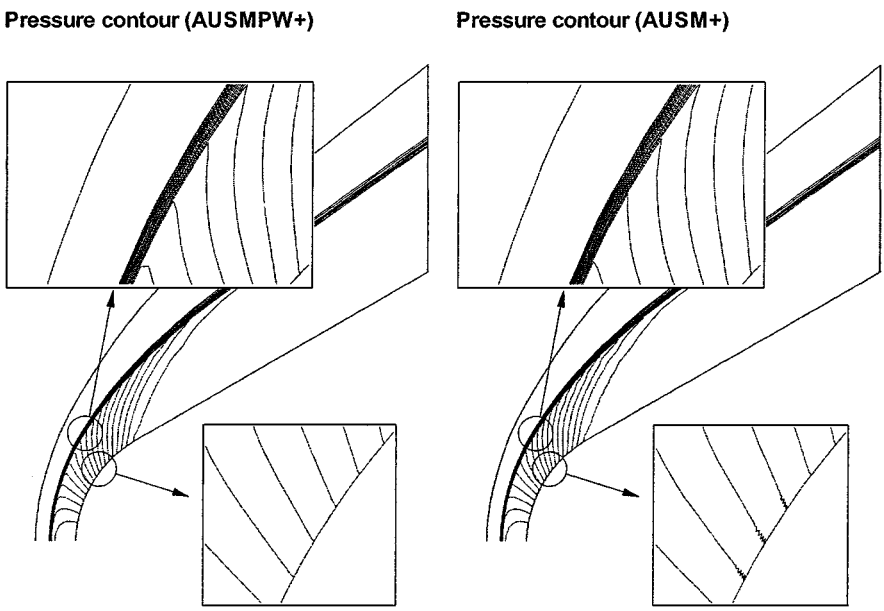

FIG. 27. Comparison of pressure distributions (AUSMPW+, AUSM+) around a nonequilibrium blunt wedge.

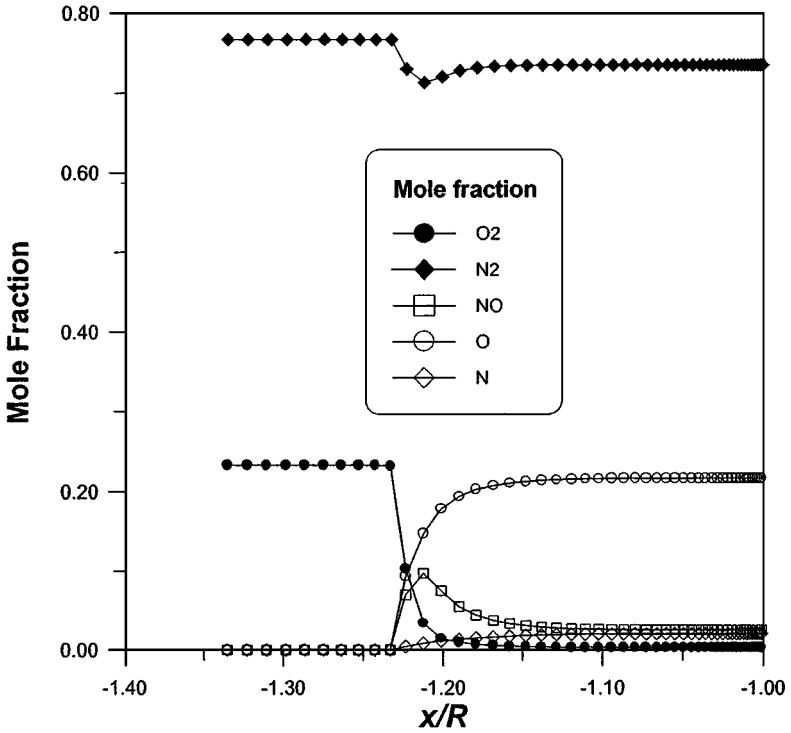

FIG. 28. Distribution of species along the stagnation streamline.

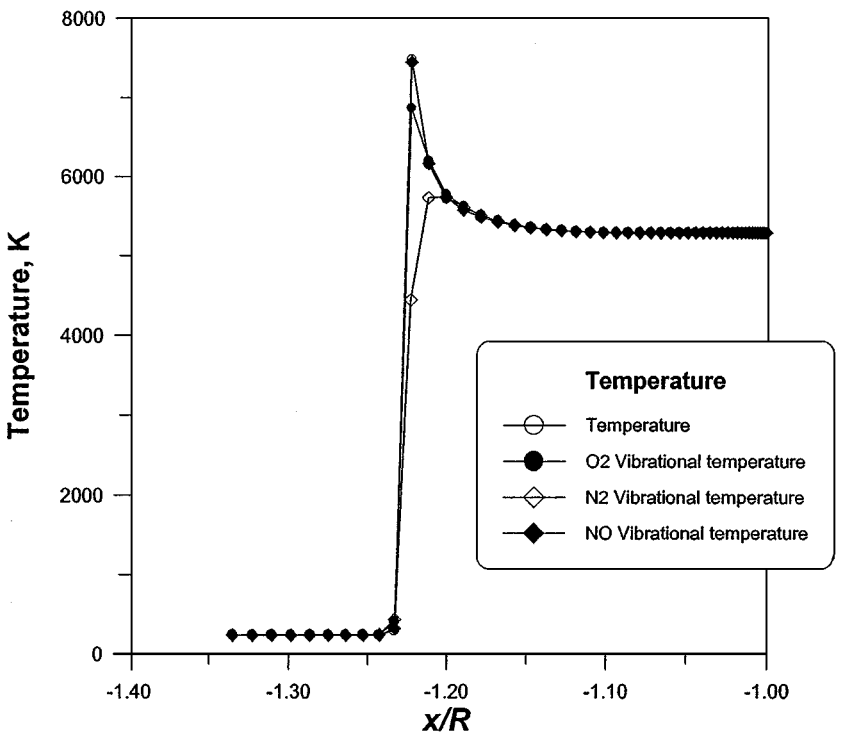

FIG. 29. Distribution of vibrational temperature along the stagnation streamline.

reduced, compared to the results in Section 6.3. Oscillations around the shock or a wall, however, are still observed, whereas AUSMPW+ does not exhibit such behavior as in the case of unstructured grids. Unlike the case of equilibrium flow, the result of AUSM+ in nonequilibrium flow shows no oscillation around the shock. This can be explained by the role of the source term in the nonequilibrium gas. As can be seen in Figs. 28 and 29, the source term is active to damp out oscillations in the transition region between the frozen and equilibrium states. Figure 26 confirms again a good convergence characteristic of AUSMPW+. Figure 28 shows the mole fraction distribution of each species along the stagnation streamline. It can be seen that oxygen is almost dissociated, and AUSMPW+ calculates a highly dissociated flow without any difficulty. Figure 29 presents the temperature distributions of each species along the stagnation streamline.

7. CONCLUSIONS

As a robust, accurate, and efficient numerical flux function to compute hypersonic flows, the AUSMPW+ scheme is proposed. The AUSMPW+ scheme, an improved version of AUSMPW, is designed to enhance the accuracy and computational efficiency in capturing oblique shock and to eliminate physically unacceptable expansion shocks. Although AUSM+ is excellent in many respects, it shows overshoots or oscillations behind shocks and near a wall. AUSMPW+ uses weighting functions based on pressure to reflect both properties of a cell interface. Exploiting these functions properly, AUSMPW+ successfully eliminates oscillations and overshoots without compromising accuracy and computational efficiency. In addition, grid dependency is reduced and convergence behavior is improved.

With the newly defined numerical speed of sound satisfying the stationary oblique shock equations, AUSMPW+ is able to capture a stationary oblique shock in one cell interface in shock-aligned grids. In non-shock-aligned grids, the newly proposed speed of sound and Mach number and pressure splitting functions of AUSMPW+ avoid extra numerical dissipation to yield more accurate results. Numerous computations from supersonic frozen flows to hypersonic nonequilibrium flows confirm the characteristics of AUSMPW+.

ACKNOWLEDGMENTS

This research was supported in part by a grant from the BK-21 Program for Mechanical and Aerospace Engineering Research at Seoul National University and a grant from the Korea Science and Engineering Foundation (Grant 98-0200-14-01-3). The authors appreciate the referees for their careful and rigorous comments on this manuscript.

REFERENCES

1. C. Park, *Interaction of Spalled Particles with Shock Layer Flow*, AIAA Paper 99-0353 (AIAA Press, Washington, DC, 1999).
2. J. L. Steger and R. F. Warming, Flux vector splitting of the inviscid gasdynamic equations with application to finite-difference methods, *J. Comput. Phys.* **40**, 263 (1981).
3. B. Van Leer, Flux-vector splitting for the Euler equation, *Lecture Notes Phys.* **170**, 507 (1982).
4. J. Gressier, P. Villedieu, and J.-M. Moshetta, Positivity of flux vector splitting schemes, *J. Comput. Phys.* **155**, 199 (1999).
5. P. L. Roe, Approximate Riemann solvers, parameter vectors and difference schemes, *J. Comput. Phys.* **43**, 357 (1981).

6. J. J. Quirk, A contribution to the great Riemann solver debate, *Int. J. Numer. Meth. Fluids* **18**, 555 (1994).
7. B. Einfeldt, On Godunov-type method for gas dynamics, *SIAM J. Numer Anal*. **25**(2), 294 (1988).
8. M. S. Liou and C. J. Steffen Jr., A new flux splitting scheme, *J. Comput. Phys.* **107**, 23 (1993).
9. M. S. Liou and Y. Wada, *A Flux Splitting Scheme with High-Resolution and Robustness for Discontinuities*, AIAA Paper 94-0083 (AIAA Press, Washington, DC, 1994).
10. M. S. Liou, A sequel to AUSM: AUSM+, *J. Comput. Phys.* **129**, 364 (1996).
11. K. H. Kim and O. H. Rho, An improvement of AUSM schemes by introducing the pressure-based weight functions, *Comput. Fluids* **27**(3), 311 (1998).
12. K. H. Kim and O. H. Rho, An improvement of AUSM schemes by introducing the pressure-based weight functions, in *The Fifth Annual Conference of the Computational Fluid Dynamics Society of Canada (CFD 97)*, Vol. 5, pp. 14-33–14-38, 1997.
13. J. R. Edwards, *A Low-Diffusion Flux-Splitting Scheme for Navier-Stokes Calculations*, AIAA Paper 95-1703-CP (AIAA Press, Washington, DC, 1995).
14. S. Srinivasan, J. C. Tannehill, and K. J. Weilmuenster, *Simplified Curve Fits for the Thermodynamic Properties of Equilibrium Air*, NASA RP-1181, Aug. 1987.
15. R. N. Gupta, K. P. Lee, R. A. Thompson, and J. M. Yos, *Calculations and Curve Fits of Thermodynamic and Transport Properties for Equilibrium Air to 30000 K*, NASA RP-1260, 1991.
16. T. K. S. Murthy, *Computational Methods in Hypersonic Aerodynamics* (Kluwer Academic, Dordrecht, 1991).
17. C. Park, Review of chemical-kinetic problems of future NASA missions, I: Earth entries, *J. Thermophys. Heat Transf.* **7**(3), 385 (1993).
18. M. S. Liou, Mass flux schemes and connection to shock instability, *J. Comput. Phys.* **160**, 623 (2000).
19. S. Tatsumi, L. Martinelli, and A. Jameson, Design, implementation and validation of flux limited schemes for the solution of the compressible Navier–Stokes equations, *AIAA J.* **33**, 252 (1995).
20. Reference deleted in proof.
21. Reference deleted in proof.
22. Reference deleted in proof.
23. Reference deleted in proof.
24. Reference deleted in proof.
25. Reference deleted in proof.
26. Reference deleted in proof.
27. Reference deleted in proof.
28. Reference deleted in proof.
29. Reference deleted in proof.
30. Reference deleted in proof.